POLITECNICO
MILANO 1863

SCUOLA DI INGEGNERIA INDUSTRIALE
E DELL'INFORMAZIONE

Critical assessment of RANS turbulence models in predicting the turbulent flow past a rectangular cylinder.

Tesi di Laurea Magistrale in
Aeronautical Engineering - Ingegneria Aeronautica

Lorenzo Pierpaoli, 10614970

Advisor:
Prof. Maurizio Quadrio

Co-advisors:
Dr. Alessandro Chiarini

Academic year:
2022-2023

Abstract: We investigate the capability of RANS models in simulating the turbulent flow past a rectangular cylinder with chord-to-thickness ratio 5 : 1, also known as the BARC benchmark, at the relatively low Reynolds number of $Re = 3000$. Four turbulence models are considered, and their performances are compared to available DNS results. Despite the simple geometry, this flow is particularly challenging as it faces a laminar separation, a shear layer that becomes unstable, forward and reverse boundary layers and several recirculating regions. The considered RANS models predict fairly well the average drag coefficient, but fail in determining the main features of the mean flow. Some models fail also in predicting the wake vortex shedding. The terms of the budget equation for the turbulent kinetic energy are used to critically assess the performances of the models and highlight their limits. Such information is valuable for the fine-tuning and development of turbulence models in these complex separating and reattaching flows.

Key-words: Turbulence models, bluff bodies, URANS

1. Introduction

Researchers investigating the aerodynamic characteristics of complex geometries have benefited in recent years from the increase in computational power at their disposal; the use of numerical simulations has become a viable alternative to difficult experimental tests. The computational approach can offer various options, differing from each other in mathematical formulation, accuracy and time and power requirements. Three main computational approaches can be identified and will be presented in order of decreasing cost and reliability: Direct Numerical Simulations (DNS), Large-Eddy Simulations (LES) and Reynolds Average Navier-Stokes models (RANS) (Pope, 2000). The Direct Numerical Simulation (DNS) of the Navier-Stokes equations is the most reliable but expensive approach. DNS solves the exact equations of the flow without modelling. This type of analysis is generally reserved for fundamental studies and its application is limited by the large cost proportional to the cube of the Reynolds number (Pope, 2000). LES simulations are a cheaper alternative to DNS simulation, resolving only the larger dynamically significant turbulent scales and resorting to modelling to account for the effect of the smaller ones. The approach with the lowest cost are RANS simulations, in which the Reynolds Averaged Navier-Stokes equations, characterized by the decomposition of the velocity field in mean and fluctuating part, are solved for the mean components of the velocity, while the contribution of the fluctuating parts, in the form of the Reynolds-stresses, is modelled either via the turbulent viscosity hypothesis or directly modelling the transport equations for the stresses (Pope, 2000). In terms of computational cost, Schafer (2006) suggest that,

for the simulation of the aerodynamics of a whole plane, with a theoretical desired computing time of 1 hour, the Flop rate required for the use of RANS models would be approximately $10^9 - 10^{11}$, while for LES would be $10^{13} - 10^{17}$ and for DNS equal to $10^{19} - 10^{23}$.
The computational power available to designer and engineers, despite constantly increasing in time, is still limited, for this reason the RANS approach is currently the only viable method when working on complex geometries or when requiring a large number of simulations. The use of this approach suffers from the intrinsic limitations and inaccuracies that characterize the Reynolds Averaged equations and the turbulence model that are used to account for the contribution of the Reynolds stresses. One example are the well known inaccuracies of the Boussinesq or "turbulent viscosity" hypothesis (Pope, 2000) that is utilized in most of the commonly used turbulence models. It should also be highlighted that the derivation of the turbulence models' equations is often empirical in nature, one notable example is the Spalart Allmaras model (Spalart & Allmaras, 1992), that introduces an empirical budget equation for the eddy turbulent viscosity by "*assembling dimensionally correct terms that together constitute a plausible transport equation for* ν_t". These models are often developed to simulate specific conditions such as free shear flows or aerodynamic profiles with small curvatures. For this reason their empirical coefficients are tweaked to improve the performance in the specific case for which they are developed with a possible consequent loss of versatility and applicability to other types of flows. In addition, in the case of low Reynolds number flows, the accuracy of these methods is limited (Bauer & Tyacke, 2022). However, RANS simulations may provide good results if properly tuned for the case of interest. One example is presented in Catalano & Tognaccini (2011), the authors were able to obtain accurate RANS simulations' results compared to LES imposing the known transition position of the laminar shear layer in the study of low Re flow around an airfoil.
Given the mentioned shortcomings of this methodology, in order to asses the ability of RANS simulations to achieve accurate solutions when applied to complex flows, a process of validation is required. This process consists in simulating well known flows for which considerable information is present in literature, the available experimental data are then used as a benchmark to evaluate the accuracy of the models implemented. The aim of this is to identify the best turbulence models for each simple flow case and, at the same time, determine the range of applicability of the RANS models. Various quantities can be considered for these comparisons such as velocity profiles, spreading rates and pressure coefficient profiles; a few examples for this procedure can be found in Bardina *et al.* (1997); Delibra *et al.* (2009); Li *et al.* (2016). This validation approach based on the comparison to experimental results, as indicated in Williams *et al.* (2020) and Spalart (2000), may present some criticalities, such as the available Reynolds numbers, the effect of the incoming turbulence level that is hard to measure and the influence of small inaccuracies in the model geometries.
Thanks to the large increase of the computational power and the development of efficient codes, over the last years DNS simulations at relatively large Reynolds numbers have appeared and can be used as a reference for the validation of the RANS models, overcoming the limitations previously mentioned.
The use of this type of numerical simulations allows for the resolution of all significant motion scales, thus offering a complete and detailed understanding of the flow features. The extensive amount of information delivered by this computations can be used as reference value for the validation of turbulence models used in RANS simulations or to evaluate the accuracy of LES results. In this study a DNS simulation is used to evaluate the accuracy of four turbulence models ($k - \epsilon$ (Launder *et al.*, 1975) (indicated with KE), Launder Sharma $k - \epsilon$ (Launder & Sharma, 1974) (LSKE), $k - \omega$ SST (Menter, 1994) (KWSST) and Spalart Allmaras with Rotational/Curvature Correction (Zhang & Yang, 2013) (SARC)) in a low Re separating and reattaching turbulent flow. The comparison is based not only on the standard flow characteristics such as velocity profiles and pressure and friction coefficients that are commonly used in the validation processes, but also on the analysis of the components of the mean turbulent kinetic energy budget. This allows for the evaluation of the difference between DNS and RANS prediction of the specific components of the budget, in order to identify those that are not estimated correctly by the models. This comparison is only made possible by the exact information regarding the velocity field obtained in the DNS study and would be impossible in the case of an experimental reference solution, requiring an unmanageable number of velocity measurements in the flow field.
The designated flow selected in this study is the flow around a rectangular cylinder with a length-to-thickness ratio $L : D$ of $5 : 1$ at a Reynolds number based on the cylinder thickness and free-stream velocity $Re_D = U_\infty D/\nu$ of $Re_D = 3000$. As reference, we use the DNS introduced in Chiarini & Quadrio (2021). This flow configuration has been the focus of multiple studies in recent years and has been indicated in 2008 as a benchmark case with the name of BARC (Benchmark on the Aerodynamics of a Rectangular $5 : 1$ Cylinder) for the study of bluff body flows (Bruno *et al.* (2008), see https://www.aniv-iawe.org/barc-home/). The interest in this case is motivated by the complex flow structures that develop around the cylinder i.e. a laminar separation, a shear layer that become unstable, several recirculating regions, a flow reattachment and the consequent formation of two opposite boundary layers.
This complexity has been also underlined in Bruno *et al.* (2014), in which a large unexpected variation between the results obtained both in experimental and computational analysis is noted, the same variation in the results can also be observed in the numerical results published after Bruno *et al.* (2014) and summarized in Table 1.

A non negligible dispersion of the results is noted specifically for the standard deviation of the lift coefficient, the length of the recirculating region on the side of the cylinder and consequently the pressure distribution. Even the application of high accuracy methods such as LES and DNS (for low Re cases) has not lead to similar characteristics across different simulation results. Over the years, several studies have investigated the possible reasons for this variability in the experimental and computational results with inconclusive results (Bartoli *et al.*, 2011; Bronkhorst *et al.*, 2011; Xiao-bing *et al.*, 2015; Ricci *et al.*, 2017; Mannini *et al.*, 2017, 2019; Corsini *et al.*, 2022). The complex flow features for this geometry provide the opportunity to compare different simulation models and evaluate their performance in a variety of critical conditions, resulting in useful information for the field of bluff body aerodynamics (Ohya, 2014; Sun *et al.*, 2019). The aim of this work, therefore, is to provide a critical assessment of the ability of four RANS models in predicting the BARC flow at the relatively low Reynolds number of $Re_D = 3000$, using the DNS by Chiarini & Quadrio (2021) as reference. Out of the four models considered KE, KWSST and SARC were chosen due to their frequent application and use in the research field and in industry, in addition the LSKE model offers the possibility to evaluate the performance of one of the proposed modifications to the standard KE model, developed to overcome the weaknesses of this model when predicting the near wall region through the use of two damping function applied to the equations for the turbulent kinetic energy k and the dissipation ϵ (additional details are available in the Appendix A). The proposed validation approach does not only offer a method to quantify the errors of these turbulence models but introduces the possibility to identify which turbulent mechanisms (i.e. production, dissipation and diffusion of k) are not effectively predicted by the model, indicating which area of the model requires additional corrections. Given the current effort in the development of effective RANS simulations (Bush *et al.*, 2019), this approach can become a useful tool for the community in the formulation of new models.
In order to consider the effect of different inflow conditions in the RANS case in Section 3.4 the effect two different inlet turbulence intensities is analyzed while in Section 3.5 the flow at $Re_D = 3 \times 10^5$ is considered, to account for the Reynolds number effect.

1.1. Reference Flow

In this work we consider the incompressible flow past a rectangular cylinder with aspect ratio $AR = L/D = 5$, where L and D are the cylinder length and thickness. This geometry is defined as the "Benchmark on the Aerodynamics of a Rectangular 5 : 1 Cylinder" (BARC), introduced by Bruno *et al.* (2008). Its objective is to characterise the flow, set the standards for simulations and experiments in the turbulent regime and to promote the understanding of the flow features. The available DNS results for this flow configurations are those introduced by Cimarelli *et al.* (2018*a*) and Chiarini & Quadrio (2021). The second work is the most recent and well resolved DNS available and offers complete information regarding the flow structure. For this reason it will be utilised as reference for all the evaluations of the turbulence models. To set the stage Figure 1 plots the mean velocity field at $Re_D = 3000$ with U indicating the absolute value of mean velocity and Figure 2 presents the instantaneous vortical structure identified with the λ_2 criterion (Jeong & Hussain, 1995). When the flow impinges on the leading edge it separates generating a shear layers that at first is laminar and bidimensional, then a Kelvin-Helmoltz like instability ensues and leads to a breakdown into large spanwise tubes (Cimarelli *et al.*, 2018*b*). The Kelvin-Helmholtz rolls are then stretched by the mean flow and roll up generating hairpin vortices. At $x \approx -1.3$ the transition to turbulent flow is observed. For $x \geq 0$ the flow is fully turbulent and the stretched hairpin vortices break down into small scale elongated streamwise vortices (Chiarini *et al.*, 2022). A second separation induced by the trailing edge leads to the formation of an additional unstable shear layer and consequently of large turbulent structures.
Observing the mean flow (Fig. 1-3) three vortices can be identified on each cylinder side. Along the longitudinal side after the laminar separation originated by the leading edge a recirculating region is formed, inside which two vortices are contained. The main one, hereafter referred to as primary vortex, spans for the complete length of the recirculating region while the second one consists of a small counter-rotating vortex placed right after the leading edge and between the primary vortex and the cylinder body. At the end of the cylinder the sharp trailing edges determine the separation in the second recirculating region behind the rear surface and, moving away from the body, a large turbulent wake develops. Another feature of particular interest is the reattachment region and consequently the two boundary layers that develop from the reattachment point oriented towards the leading and trailing edges.

1.2. Previous Studies

Over the last years several works have contributed to this specific benchmark with numerical and experimental studies. A review is provided in Bruno *et al.* (2014), in which multiple simulations studies are compared with experimental results of four different studies: Shirato *et al.* (2010), Bartoli *et al.* (2011), Bronkhorst *et al.*

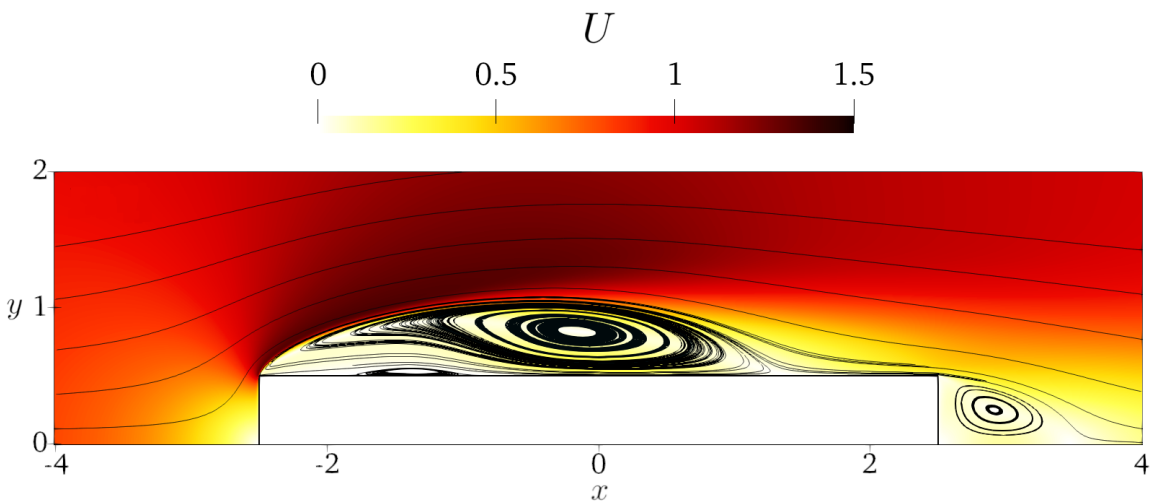

Figure 1: Mean streamlines drawn over a colormap of the magnitude of the mean velocity in the reference DNS simulation.

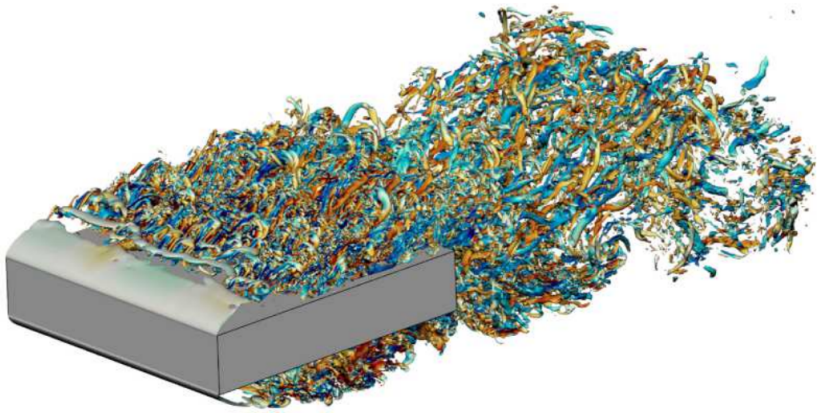

Figure 2: Instantaneous representation of isosurfaces with $\lambda_2 = -5$, coloring represents the value of streamwise vorticity ω_z with a blu to red colormap and range $-10 < \omega_z < 10$, image taken from Chiarini *et al.* (2022).

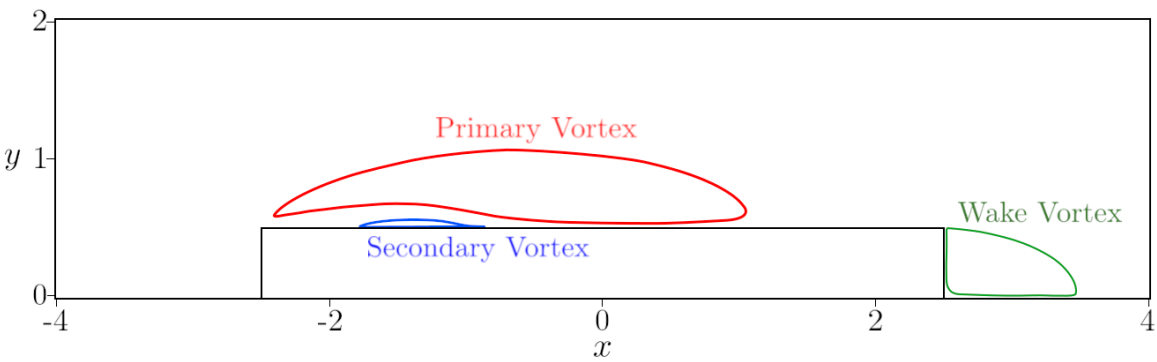

Figure 3: Vortex structures in the mean flow.

	Simulation type	Re	$(C_l)_{std}$	$\langle C_d \rangle$	f
Chiarini & Quadrio (2021)	DNS	3×10^3	0.2893[a]	0.9437	0.1274
Cimarelli *et al.* (2018*a*)	DNS	3×10^3	-	0.96	0.14
Zhang & Xu (2020)	LES	4×10^4	0.25-0.55	0.96-0.98	0.114-0.126
Nguyen *et al.* (2018)	LES	6.7×10^3	0.091	-	0.608
Patruno *et al.* (2016)	LES	5.5×10^4	0.19	1.02	0.132
Patruno *et al.* (2016)	URANS 2D	5.5×10^4	0.81	1.12	0.121

Table 1: Numerical Results Review.

[a]This value represents the $(C_l)_{rms}$

(2011) and Schewe (2013) revealing a consistent dispersion of the numerical results especially in the case of lift coefficient standard deviation $(C_l)_{std}$. This apparently simple flow has proven to be quite challenging both from the experimental and numerical point of view, to this day consistent results across different methodologies and approaches have not been achieved other than the most recent results in Corsini *et al.* (2022) comparing LES and DNS results. In order to identify the cause of this behaviour Bronkhorst *et al.* (2011) and Bartoli *et al.* (2011) investigated experimentally the causes for the unexpected asymmetrical results obtained by multiple studies. The former focused on the effect of inaccuracy in the model shape for wind tunnel test and the latter on the effect of misalignment relative to the flow direction. Additional experimental studies, investigating different factors, have been proposed and focus on the effect of turbulence intensity in the inflow (Mannini *et al.*, 2017), the accuracy in the model dimension and corner sharpness, correct alignment with the wind tunnel flow orientation and pressure tap disturbances (Bronkhorst *et al.*, 2011; Bartoli *et al.*, 2011). On the computational side the effects of spanwise discretisation (Mannini *et al.*, 2019), mesh resolution (Zhang & Xu, 2020), corner sharpness (Ribeiro, 2011), inflow condition (Ricci *et al.*, 2017) and spanwise correlation (Xiao-bing *et al.*, 2015) have been investigated with inconclusive results. The question regarding the effect of spatial discretization has been also the focus of Corsini *et al.* (2022) and an unusual strong dependence of the DNS results from the domain discretization, especially in the streamwise direction, has been observed. The importance of corner definition in the accuracy of the numerical results has been recently the subject of two comparable studies, utilizing LES and DNS simulations. Rocchio *et al.* (2020) indicates that for LES at $Re_D = 4 \times 10^4$ the introduction of even a small curvature radius to the leading edge corners increases noticeably the agreement to experimental results. In Chiarini & Quadrio (2022) this approach is replicated with DNS at $Re_D = 3000$ with different results, a small rounding of the leading edges does not lead to drastic variation of the mean flow, the change of the mean flow features is proportional to the rounding value.

In the case of lower accuracy methods, such as RANS simulations, that are the main topic of this study, the complexity of the flow itself, as previously described, can contribute to the large dispersion observed in the results. The first of multiple challenges for the turbulence models presented by this geometry is the strong variation of the mean flow direction imposed by the rectangular cylinder leading to the formation of a laminar separation bubble around the sides. The simulation of this abrupt variation of direction is affected by the known weaknesses of the modelled dissipation rate equation as addressed by Franke & Rodi (1993). The laminar separated shear layer undergoes a transition into a turbulent flow and the prediction of this complex mechanism can be challenging in RANS simulations especially when using eddy viscosity models (Aupoix *et al.*, 2011). Another critical feature that the turbulence models implemented in this study are unable to predict is the region of non-negligible negative production of turbulent kinetic energy in the shear layer, investigated for the first time in two studies by Cimarelli *et al.* (2018*a*, 2019) with DNS simulations. In Chiarini & Quadrio (2022), in which a DNS with higher level of discretisation is conducted, the size of this region and the intensity of negative production are found to be smaller and lower than what observed in Cimarelli *et al.* (2018*a*) but still present. As indicate by Yan *et al.* (2022) turbulence models are calibrated and designed to operate in TKE budget equilibrium regions, complex flows in which non equilibrium regions are originated are for this reason more problematic. The importance of accurate inlet condition is explored in more detail in Ricci *et al.* (2017) and Mannini *et al.* (2017), noting that the dimensions of the two recirculating regions generated in the BARC configuration are strongly affected by the value of the free-stream turbulence, the same sensitivity to inflow condition is required from the turbulence models in order to correctly simulate real world cases in which the inlet turbulence intensity is different from zero. In Chiarini & Quadrio (2021) the influence of the wake region and the vortex shedding frequency on the flow behaviour up to the leading edge area is presented, to correctly predict this flow turbulence models are thus required to be able to deal with fully developed turbulence and at

the same time with the complexity of a reattaching flow.
The results obtained in the previous works are here summarized to provide a reference in the evaluation of the RANS simulations. Starting from one of the main characteristics of this flow condition, as the periodic vortex shedding, the numerical analyses included in Bruno *et al.* (2014) report a frequency value included in a range $0.105 < f < 0.132$, for the experimental cases the results show a larger dispersion with a range $0.073 < f < 0.16$. This variation may be due to different flow conditions considered or inaccuracies in simulations and experimental tests. The most recent numerical studies, obtained at various Re, predict values of 0.132 when using LES and 0.121 when using URANS (Patruno *et al.*, 2016), 0.114-0.126 (Zhang & Xu, 2020) and 0.14 (Cimarelli *et al.*, 2018*a*). The effect of considerable values of inlet turbulence intensity on this parameter has been studied in Mannini *et al.* (2017) with wind tunnels tests at different turbulence intensity and by Ricci *et al.* (2017) with LES simulations. Mannini *et al.* (2017) compares six inflow conditions with turbulence intensity values from 0.7% to 13.6% and $55900 < Re < 60000$, observing that even small turbulence intensity is capable of reducing consistently the dimension of the recirculating bubbles on the sides of the cylinder, inducing a faster recovery of pressure coefficient on the walls. The Strouhal number, indicating in a smooth flow condition the frequency of the vortex is also effected: without turbulence a value of $St = 0.115$ is registered while in the turbulent cases it spans for $0.1 < St < 0.24$. Patruno *et al.* (2016) implemented a study based on LES simulation of the flow with inlet turbulence intensity equal to 2.9% and 13.6% at $Re = 5.5 \times 10^4$. Similarly to the experimental results from Mannini *et al.* (2017) the increase of turbulence intensity leads to an earlier destabilization of the shear layer and consequently to a higher shear layer curvature resulting in a shorter reattachment length. Regarding the drag coefficient the reference DNS indicates a value of $\langle C_d \rangle = 0.9425$ at $Re_D = 3000$. Similar conditions (Low Re and no inflow turbulence) are investigated by a few studies reporting the following results: 0.96 (Cimarelli *et al.*, 2018*a*), 0.96-0.98 (Grozescu *et al.*, 2011) and 0.96-0.103 (Bruno *et al.*, 2008). Other results are available but are obtained at higher Re numbers, a few examples are 1.02-1.12 (Patruno *et al.*, 2016), 0.96-0.98 (Zhang & Xu, 2020) 0.968-1.071 Mannini *et al.* (2017). Referring to the results presented in Bruno *et al.* (2014) the ensemble average of all the simulations available at that time was $\langle C_d \rangle = 1.074$. Thanks to the accuracy of the DNS simulations and the results presented it is possible to suggest that an increase in Re leads to a small increase in $\langle C_d \rangle$. Focusing on the analysis of the lift coefficient and its standard deviation Bruno *et al.* (2014) highlights the sensitivity of this last parameter to numerous numerical, modelling and simulation parameters such as the effect of dissipation, grid resolution, turbulence modelling and the different types of simulation utilized. It is also important to emphasized the different physical value of the standard deviation calculated from a scale resolving model, in which physical realizations of the flow are considered and the results obtained by an averaged method such as the RANS approach. As previously noted the ensemble average presented in (Bruno *et al.*, 2014) for the lift coefficient is slightly different from zero with a value of $\langle C_l \rangle = -0.0141$ while the same review reports an ensemble average of the lift coefficient standard deviation $(C_l)_{std} = 0.65$ and with values included in the range $0.108 < (C_l)_{std} < 1.46$. The results presented after the publication of (Bruno *et al.*, 2014) are indicated in Tab. 1 and are included in the range $0.091 < (C_l)_{std} < 0.81$.
It should be noted that in the development of accurate LES simulations, despite all the limitations previously presented, significant progress has been made in Crivellini *et al.* (2022) in which a high-order discontinuous Galerkin method has been applied to implicit large eddies simulations at $Re_D = 3000$ obtaining for the first time good agreement with the DNS results by Chiarini & Quadrio (2021) with a largely inferior computational cost.

2. Numerical Methods

In this study the flow around a rectangular cylinder is used to compare the performance of four different turbulence models. The reference solution obtained with a DNS simulation Chiarini & Quadrio (2021) is used to evaluated the results of the URANS simulations implemented as it represents the most recent and accurate simulation available, having a higher mesh discretization compared to the previous work from Cimarelli *et al.* (2018*a*).
The incompressible Navier Stokes equations that are solved directly in the reference DNS study are here presented, this approach does not require any additional closure model but very fine grids and small time integration intervals need to be utilized in order to obtain an accurate solution.

$$\begin{cases} \nabla \cdot \boldsymbol{u} = 0 \\ \dfrac{\partial \boldsymbol{u}}{\partial t} + \boldsymbol{u} \cdot \nabla \boldsymbol{u} = -\nabla p + \dfrac{1}{Re} \nabla^2 \boldsymbol{u}. \end{cases} \tag{1}$$

In the case of URANS simulations the velocity vector is decomposed in its mean and fluctuating parts:

$$\{ \boldsymbol{u} = \overline{\boldsymbol{u}} + \boldsymbol{u}' \tag{2}$$

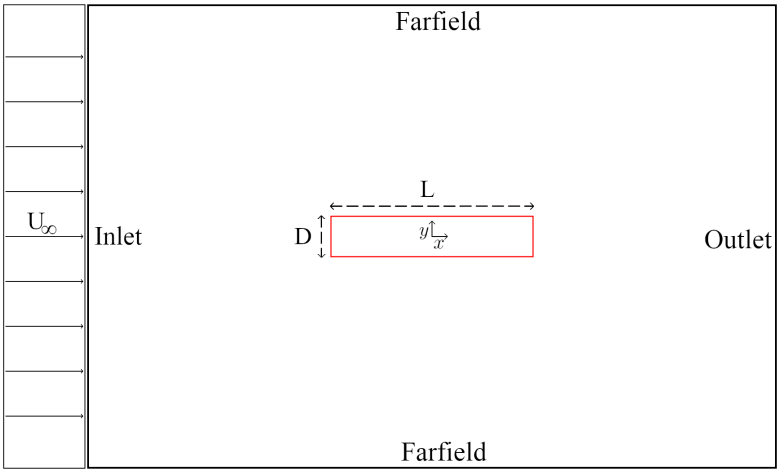

Figure 4: 2D computational domain

Where the overline operator $\overline{(\cdot)}$ indicates the averaging operation. The incompressible RANS equations, presented here, are solved for the mean component and require the use of one of the chosen turbulence models in order to account for the contribution of the Reynolds Stresses and achieve closure (a more detailed presentation of each turbulence model is included in Appendix A).

$$\begin{cases} \nabla \cdot \overline{\boldsymbol{u}} = 0 \\ \dfrac{\partial \overline{\boldsymbol{u}}}{\partial t} + \overline{\boldsymbol{u}} \cdot \nabla \overline{\boldsymbol{u}} = -\dfrac{1}{\rho} \nabla \overline{p} + \nu \nabla^2 \overline{\boldsymbol{u}} - \nabla \cdot \overline{(\boldsymbol{u}'\boldsymbol{u}')} \end{cases} \tag{3}$$

A Cartesian reference system is utilised to describe the domain, with the x-axis aligned with the undisturbed flow, the y-axis aligned to the cross stream direction and the z-axis along the span-wise direction. The value of the Re number used to specify the flow condition is based on the thickness value and is calculated as $Re_D = DU_\infty/\nu$, with U_∞, the velocity imposed at far-field. All quantities considered are adimensionalized with U_∞ and D.
The computational domain considered is the same as the reference DNS study from Chiarini & Quadrio (2021), it extends in the stream-wise direction for $-22.5 < x < 40$, in the cross stream direction for $-21 < y < 21$ and for $-2.5 < z < 2.5$ in the spanwise direction. For the 2D unsteady RANS simulation the same domain is used in the x and y direction (Figure 4). The cylinder is placed at the origin of the domain at $-2.5 < x < 2.5$ and $-0.5 < y < 0.5$.
The boundary condition imposed are fixed undisturbed velocity at the inlet and far-field equal to (U_∞, 0, 0) and an homogeneous Neumann condition at the outlet. For the pressure a fixed value is imposed at the outlet and an homogeneous Neumann condition is used at the inlet and at the far-field.
For the URANS simulations, two Reynolds numbers Re_D have been considered: $Re_D = 3000$ and $Re_D = 3 \times 10^5$. The former to have an accurate comparison to the DNS case and the latter to evaluate the sensitivity to the Re number of this type of simulation and the different characteristics and flow structures between a low and a high Re conditions. The incompressibile Reynolds Averaged Navier Stokes equation are discretized with a cell centred finite volume scheme in the OpenFOAM software. Time discretization is obtained with the Crank-Nicolson second order scheme. The PISO numerical algorithm has been used to solve the discretized equations, with two correction cycles. The gradient and divergence terms are discretized with the second order Gauss theorem, gradient terms utilize a linear interpolation while divergence terms employ a TVD scheme. Similarly for the laplacian terms the Gauss theorem with linear interpolation is used. Mean values are obtained over a time of 1 period of the periodic oscillation of lift coefficient. Four different turbulence models have been utilised and compared in this study:KWSST, SARC, KE and LSKE. The meshes for both the URANS cases have the same pattern of refinement of the DNS case but with different expansion rates. For the $Re = 3000$ meshes the finest element dimensions are Δx=Δy=0.003 obtaining a maximum y^+ for the first cell below 1. From coarse to fine the meshes consist of 60758, 121920 and 245952 elements. For the simulations utilising the LSKE, due to specific requirements regarding the first cell height, meshes with Δx=Δy=0.008 and an average $y^+ \approx 0.8$ consisting of 73924, 106108 and 145276 elements have been used. The same structure and refinement pattern is kept for the meshes used in the simulations run at $Re = 3 \times 10^5$ with the finest elements of dimension Δx=Δy=0.0006 obtaining an average $y^+ \approx 10$. From coarse to fine the meshes consist of 133068, 212196 and 358322 elements. A fixed time-step is chosen for each simulation to maintain the CFL number below 1. The same pressure and velocity boundary condition are utilised for RANS and DNS simulations.

In regards to the choice of turbulence models considered, the KWSST model has been chosen due to its success in similar studies (Bardina *et al.*, 1997; Li *et al.*, 2016; Singh *et al.*, 2020), with results that are comparable to experimental data. The KE model is a standard two equation model, although its limits are well known it still finds common use in the industrial sector; in this study it is also used as a comparison its Launder Sharma variant. The LSKE model is a low Reynolds modification of the KE model designed to deal with the shortcomings of the original one, especially in the near wall region. Four additional coefficients are added in order to limit the value of dissipation at the wall, decrease the value of turbulent viscosity through the viscous sub layer in accordance to the Van Driest model and provide damping to the production at the wall. This turbulence model offers the possibility of comparing the flaws of the standard KE (Shimada & Ishihara, 2002) with a specific model modified for low Re flows and to be able to reduce the effect of excessive TKE observed around shear layers. The rotational and curvature correction utilised in the Spalart Allmaras (SA) model is the one introduced by Zhang & Yang (2013), the production term in the standard SA equation is multiplied for an empirical rotation function, identically to the Spalart and Shure correction in which it is required to evaluate the Lagrangian derivative of the strain rate tensor, in this case the empirical rotation function is calculated using the Richardson number, allowing for more efficient simulations with results that are as accurate as the Spalart and Shure correction. Due to the nature of the flow, with its strong changes of mean flow direction this model has been preferred to the standard Spalart Allmaras.
For the implementation of the turbulence models additional boundary conditions are required: at the inlet and at the farfield the value of k, ϵ, ω e $\tilde{\nu}$ are imposed, while at the outlet an homogeneous Neumann Boundary condition is applied. On the surface of the cylinder k and $\tilde{\nu}$ are imposed equal to zero, ω is imposed with the Menter's condition ($\omega_{wall} = \frac{6\nu_{wall}}{\beta_1 y^2}$, where y indicates the height of the first cell) while for the dissipation rate a zero gradient boundary condition is imposed. A limitation of the OpenFOAM software must be considered, specifically in the imposition of the ϵ and k values, to avoid divergence due to a division by zero the value of k or ϵ equal to 10^{-7} may be used in place of $k = \epsilon = 0$

	Inlet	**Outlet**	**Farfield**	**Cylinder**
$\boldsymbol{k}$	fixedValue	zeroGradient	fixedValue	fixedValue=0
$\boldsymbol{\omega}$	fixedValue	InletOutlet	fixedValue	fixedValue (Menter)
$\boldsymbol{\epsilon}$	fixedValue	zeroGradient	fixedValue	zeroGradient
$\boldsymbol{\tilde{\nu}}$	fixedValue	zeroGradient	fixedValue	fixedValue=0
$\boldsymbol{p}$	zeroGradient	fixedValue	zeroGradient	zeroGradient
$\boldsymbol{U}$	fixedValue	fixedValue	fixedValue	noSlip

Table 2: Boundary Conditions at $Re_D = 3000$

3. Results

3.1. Time Averages

The first analysis of the simulations is based on the evaluation of the average aerodynamic coefficients and temporal characteristics. The results obtained by Chiarini and Quadrio (2021) presented in Table 3 are used as benchmark to evaluate the performance of the four turbulence models implemented.
The $\langle - \rangle$ symbol indicates, in the case of 2D URANS, time averaged values while in the case of DNS results an additional span-wise average is considered. All URANS simulations, as expected due to the symmetric flow condition, achieve an average lift coefficient close to zero, however the amplitude of the oscillation of this coefficient varies among the models. The KWSST and LSKE models obtain much larger root mean square values of the lift coefficients compared to the DNS, while the results from the KE models under-estimate the reference values. All models quite accurately predict the drag coefficient, with the KE result being the most precise, and the LSKE resulting in the largest overprediction, exceeding the reference value by 13.3%, a similar behaviour is noted also for the KWSST case. The non stationary behaviour of the flow condition is observed for all the two-equation models while the simulations implemented with the SARC model yields a stationary flow with negligible oscillations, this result is in line with Mannini *et al.* (2010) in which a stationary behaviour is obtained when using the Edwards-Chandra modification of the Spalart Allmaras model (Edwards & Chandra, 1996), the possible reason for this behaviour is the overestimation of the eddy viscosity in the wake region

that damps the detachment of the vortices. The vortex shedding frequency f is underestimated by all the non-stationary URANS simulations, with the KWSST and LSKE models being the most accurate with an error of 13.7% and 13.8%. In all simulations the drag coefficient oscillation frequency is observed to be equal to $2f$.

	f	$\langle C_l \rangle$	$(C_l)_{rms}$	C_l **extremes**	$\langle C_d \rangle$	$\Delta\langle C_d \rangle$
DNS	0.1274	-0.0155	0.29	+0.762 -0.913	0.9425	-
KE	0.0907	1.79×10^{-4}	0.165	± 0.235	0.931	-1.2%
LSKE	0.1097	2.13×10^{-4}	0.741	± 1.050	1.068	+13.3%
KWSST	0.1099	1.33×10^{-3}	0.856	± 1.208	1.045	+10.8%
SARC	-	-2.44×10^{-06}	3.11×10^{-6}	$(+0.08; -0.57) \times 10^{-5}$	0.917	-2.71%

Table 3: Mean aerodynamic coefficients and vortex sheddig characteristics

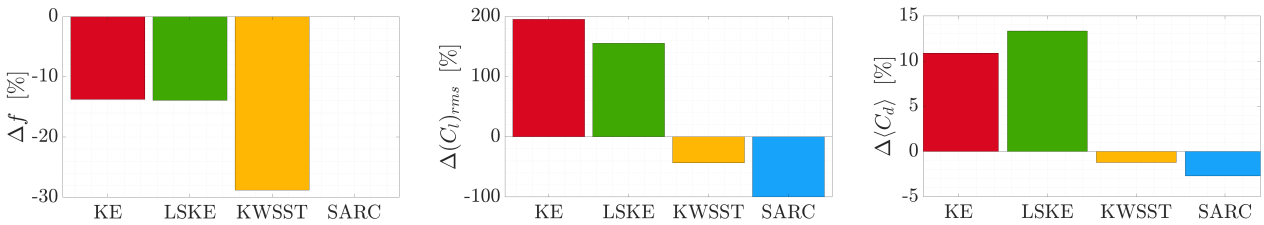

Figure 5: Percentage difference of the URANS simulated frequency, lift coefficient root mean square and mean drag coefficient compared to DNS results.

3.2. Mean Flow

3.2.1. Recirculating regions

The time averaged flows obtained from the URANS simulations are now compared to the results of the reference DNS. The velocity and the pressure field are presented in Figures 6 and 7, the details regarding the predictions of the different turbulence models used are presented in Table 4.
The DNS result predicts a symmetric flow with three vortices on each cylinder side (Figure 3), two along the cylinder's longitudinal side and one in the wake region. Inside the main recirculating region, along the cylinder side, the "Primary vortex" develops from the interaction of the flow with the cylinder leading edge and spans for a length of 3.95 with its centre point, identified with the stagnation point $U = V = 0$, at $(-0.143, 0.93)$. A second smaller counter-rotating vortex ("Secondary vortex") is located within the separated region after the LE square corners in the inverse boundary layer region caused by the primary vortex, its centre of rotation is located at $(-1.3, 0.541)$. The third vortex develops in the wake behind the cylinder with its centre at $(2.93, 0.25)$. All the models implemented can account for the primary vortex with a variable degree of accuracy, being the easiest one to identify due to the forced separation induced by the leading edge corners. In contrast none are able to predict the formation of the secondary one. The DNS reference study or the available LES simulations (Patruno *et al.*, 2016; Bruno *et al.*, 2008) predict a complex main recirculating region. In Bruno et al (2008) the topology of this region is extensively described, three areas are identified: two vortices and one section indicated as "inner region" located between the two. As a consequence the primary vortex presents a teardrop shape, that can only be predicted by the LSKE model while the other URANS result present a much simpler elliptical vortex shape. The model that more closely predicts the position of the primary vortex centre is the LSKE model, with its position at $(-0.289, 0.82)$, followed by the KWSST model. The SARC simulations are quite inaccurate, predicting a smaller vortex with the center placed closer to leading edge. The extension of these vortices can be compared observing the position of the reattachment points, indicated with $x_{e,1}$ in Table 4. The KE model proves to be the most accurate together with the results of the LSKE model with an estimated length of respectively 3.92 and 4.01 units compared to the DNS value of 3.95. The SARC model predicts a much smaller primary recirculating region than expected, with a length of 3.452 units while the KWSST model performs the worst, overestimating the vortex length by 0.45 units. Comparing the maximum extension in the y direction of the recirculating region the DNS simulations predicts a region that extends up to $y = 1.058$ while

		DNS	KE	LSKE	KWSST	SARC
Primary v.	$x_{s,1}$	-2.5	-2.5	-2.5	-2.5	-2.5
	$x_{e,1}$	1.45	1.42	1.51	1.90	0.952
	L_1	3.95	3.92	4.01	4.40	3.452
	(x_c, y_c)	$(-0.143, 0.83)$	$(-0.631, 0.81)$	$(-0.289, 0.82)$	$(-0.293, 0.817)$	$(-1.435, 0.712)$
Secondary v.	$x_{s,2}$	-1.85	–	–	–	–
	$x_{e,2}$	-0.95	–	–	–	–
	L_2	0.9	–	–	–	–
	(x_c, y_c)	$(-1.3, 0.541)$	–	–	–	–
Wake v.	$x_{s,3}$	2.5	2.5	2.5	2.5	2.5
	$x_{e,3}$	3.48	3.55	3.195	3.21	3.78
	L	0.98	1.05	0.695	0.71	1.28
	(x_c, y_c)	$(2.93, 0.25)$	$(2.85, 0.265)$	$(2.751, 0.257)$	$(2.748, 0.263)$	$(2.99, 0.26)$

Table 4

for the KWSST up to $y = 1.029$, SARC up to $y = 0.889$, KE up to $y = 1.003$ and LSKE up to $y = 1.042$. The turbulence models, in their prediction of the shear layer, tend to overestimate the curvature imposed to the flow and the rotational acceleration around the leading edge corner leading to thinner recirculating region, the LSKE model shows the most accurate result compared to the reference flow. The results regarding the wake region differ noticeably among the chosen models. The reference simulation predicts a vortex centered in $(2.93, 0.25)$ and that extends up to $x = 3.48$. The closest prediction of this value is offered by the KE model that quite accurately indicates a length of 1.05 units compared to the 0.98 of the DNS. This parameter is also affected by the curvature imposed to the flow around the TE corners with the KWSST and LSKE models imposing a stronger rotational acceleration inducing a shorter recirculating region. Comparable results are indicated by the KWSST and LSKE models, with the latter being slightly more precise in the positioning of the vortex center. The SARC model, although quite accurate in the identification of the center point, predicts a longer recirculating region of 1.28 units.

3.2.2. Aerodynamic forces

The forces developed over the cylinder longitudinal sides by the flow have been analyzed observing the mean pressure $\langle c_p \rangle$ and wall shear stress $\langle c_f \rangle$ coefficients distribution over the body surface, that are rendered dimensionless with $\frac{1}{2}\rho U_\infty^2$. The two coefficients obtained by the different simulations are plotted in Figure 8. According to the DNS results, the friction coefficient assumes a negative value at the leading edge of the cylinder, than increases up to a value of $\langle c_f \rangle \approx 0$ where it stabilises, and for $1.87 < x < -0.91$ holds a slightly positive value. After this portion it decreases to its local minimum value of $\langle c_f \rangle = 0.0118$ at $x = 0.319$ and than increases towards its maximum at the trailing edge. This behaviour is a reflection of the flow structures developed in the region close to the wall: the counter-rotating vortex, even if characterised by a slow rotation, is responsible for the region of positive friction coefficient; the minimum value is instead a consequence of the fast reverse flow induced by the primary vortex. None of the turbulence models implemented is able to predict the secondary vortex and its effect on the friction coefficient, this result is in line with the URANS simulations available in literature for this flow: in Patruno *et al.* (2016) the KWSST model is not capable of identifying this feature while in Mannini *et al.* (2010) in which the Spalart Allmaras model modification proposed by Edwards and Chandra and the Linearised Explicit Algebraic model (which is the linear truncation of the Explicit Algebraic Reynolds Stress Model) are used, only the second model is predicting a secondary vortex. Thus, the $\langle c_f \rangle$ value at the front of the cylinder does not become positive for any URANS simulation. The LSKE model is the most accurate in the front section of the cylinder, predicting values close to the reference results up to $x \approx -1.3$, it reaches its minimum vale of $\langle c_f \rangle = -0.0134$ at $x = 0.34$ showing a similar behaviour to the DNS case but with larger negative friction coefficient. An interesting behaviour is shown by the SARC model that performs quite poorly close to the leading edge predicting a minimum value of $\langle c_f \rangle = -0.015$ at $x = -1.145$ followed by a sharp increase of the coefficient leading to a slightly positive $\Delta\langle c_f \rangle$. The drastically different behaviour in the first half of the body can be seen as a consequence of the different characteristics of the mean flow, such as the smaller recirculating region that is characterized by higher velocities close to the wall, leading to large negative value of $\langle c_f \rangle$. In the second half of the cylinder, the SARC model is instead the best performer out the models implemented showing very low values of $\Delta\langle c_f \rangle$. All the two equation models present a negative value of $\Delta\langle c_f \rangle$ for most of the body length, this indicates in the frontal region the inability to predict the slow secondary vortex, while, from the secondary reattachment point, is a consequence of the stronger negative wall

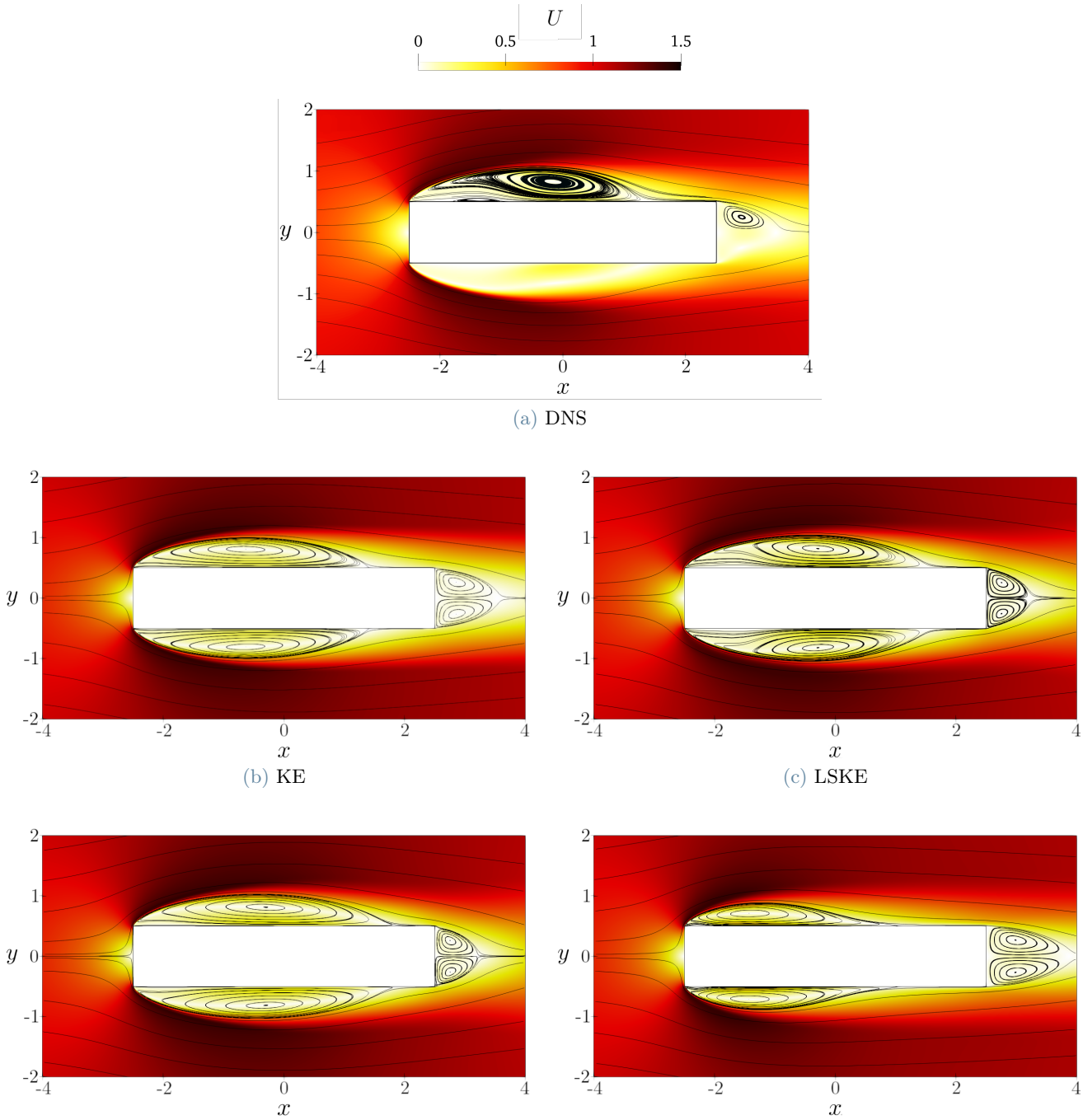

(a) DNS

(b) KE

(c) LSKE

(d) KWSST

(e) SARC

Figure 6: Mean streamlines drawn over a colormap of the magnitude of the mean velocity.

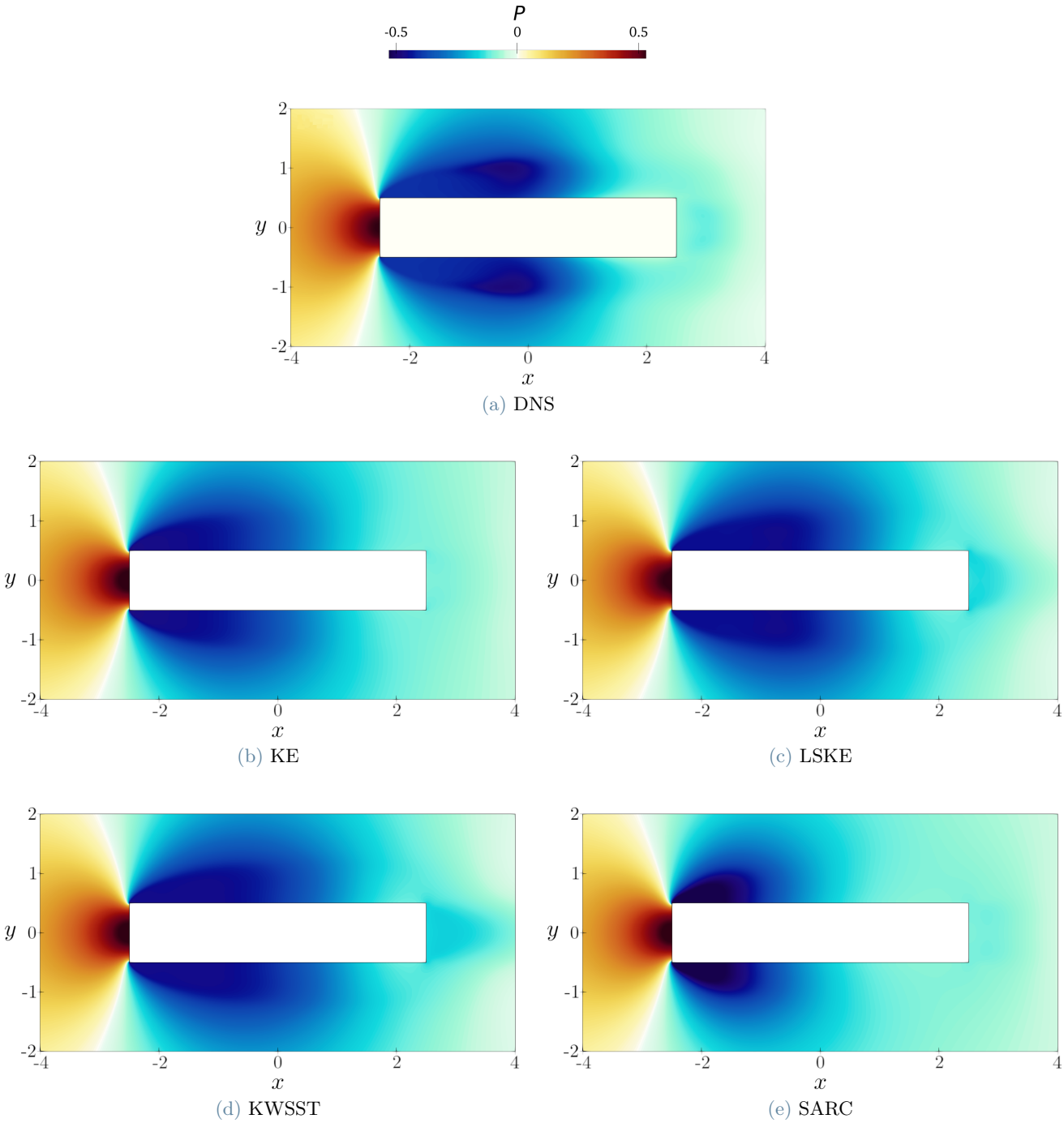

(a) DNS

(b) KE

(c) LSKE

(d) KWSST

(e) SARC

Figure 7: Colormap of the mean pressure field.

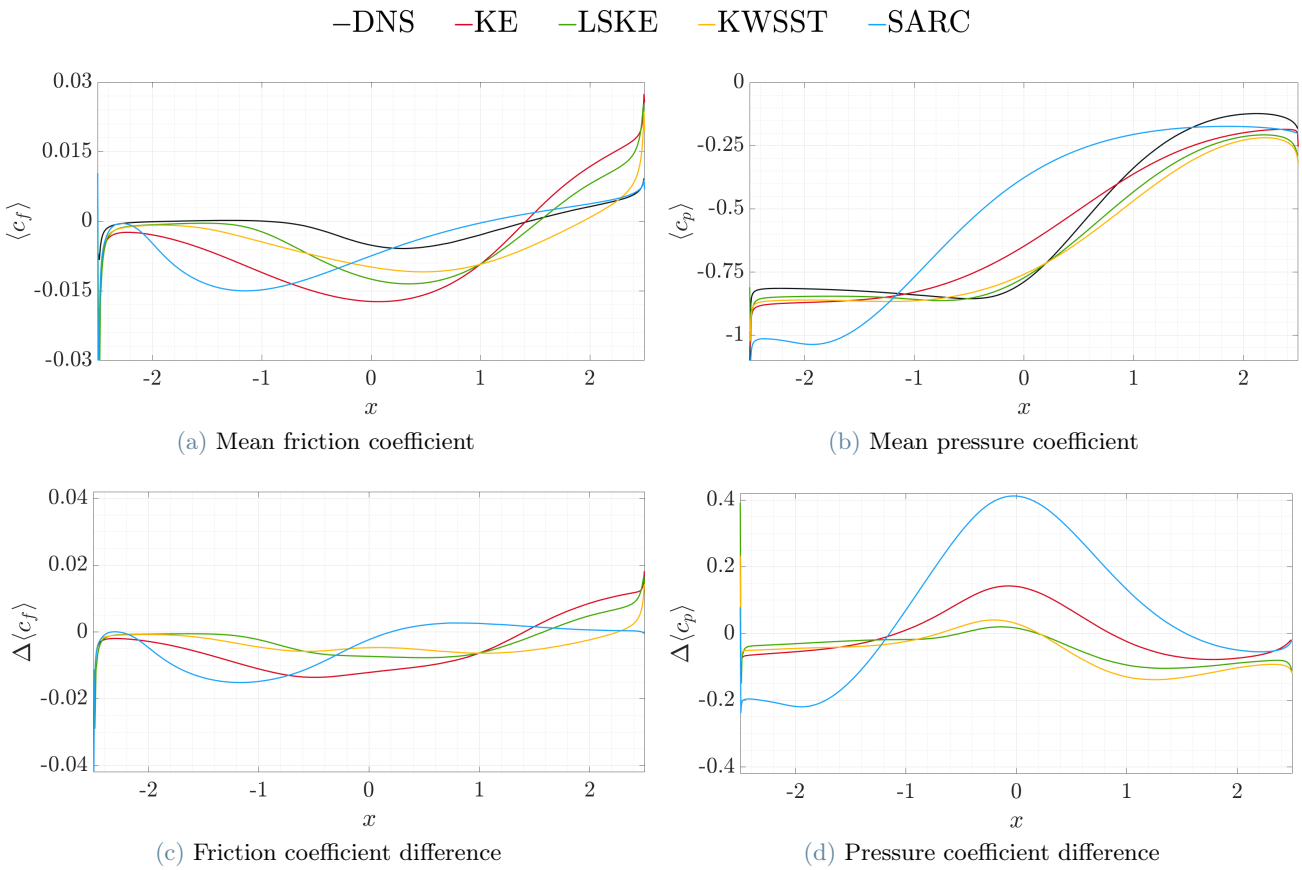

(a) Mean friction coefficient

(b) Mean pressure coefficient

(c) Friction coefficient difference

(d) Pressure coefficient difference

Figure 8: Mean pressure and friction coefficients differences from the DNS reference solution over the cylinder longitudinal side.

shear stress induced by the large separated region.
The pressure coefficient resulting from the DNS is plotted in Figure 8d. The minimum value is reached at the leading edge and it remains below zero along the whole cylinder side wall. After the sharp increase following the leading edge it maintains a slow decline towards the minimum $\langle c_p \rangle = -0.855$ at $x = -0.470$. The minimum value is the effect, on the wall, of the negative pressure inside the main recirculating region. All two-equations models are quite accurate in the evaluation of the pressure coefficient, especially the KWSST and the LSKE. These two models predict similar behaviours but with lower $\langle c_p \rangle$ values compared to the DNS in both the front and rear regions. In the central part of the body, between $-1 < x < 0.3$, all models predict a higher pressure coefficient value than the reference one. This location is interested in the DNS case by the primary vortex center and consequently by high flow velocity at the wall coupled with the pressure local minimum, on the other hand all turbulence models predict the position of the primary vortex center closer to the leading edge, thus being interested in this region by a pressure recovery and resulting in a positive $\Delta\langle c_p \rangle$ with respect to the DNS case (figure 8d). In addition, the reference case presents a fast pressure recovery after the primary vortex center that is not captured by the turbulence models, for this reason the $\Delta\langle c_p \rangle$ becomes quickly negative for $x > 0.3$. The different behaviours of the four turbulence models in the description of the flow in the rear region have been presented while discussing the dimension of the wake vortex, the analysis of the pressure coefficient over the back side of the body in Figure 9 offers additional information regarding this region of the flow. The DNS results is characterized by a higher $\langle c_p \rangle$ value than the URANS simulations and is best approximated by the SARC and standard KE model, this result is in line with the quite accurate approximation of the wake vortex center position offered by the two models. On the other hand for the KWSST and the LSKE models the wake vortex develops closer to the cylinder back side inducing a lower pressure coefficient. As indicated in the previous section these two models impose a stronger rotational acceleration to the flow around the TE corners that can be correlated to the lower pressure inside the wake vortex.

3.2.3. Velocity Profiles

In order to evaluate the ability of the models to accurately describe the velocity distribution of the flow around the body, the velocity component aligned with x has been compared across the different simulations in Figure

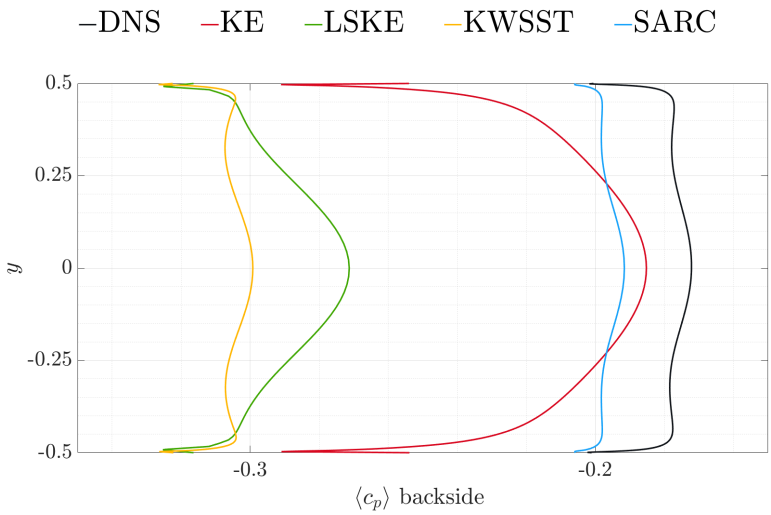

Figure 9: Mean pressure coefficient over the cylinder rear surface at $x = 2.5$.

11. Considering the variability in the position of the vortices and of the reattachment point obtained by the different turbulence models, to compare the velocity profiles (computed in the y-axis direction and spanning from the center-line up to $y = 2$) obtained at the same geometrical position for all cases would lead to an ineffective comparison. The variable distance between the investigation line and the flow features would largely effect the velocity profiles. Consequently the velocity data is gathered in each simulation at specific topological points of interest (primary vortex center, shear layer reattachment, trailing edge and wake vortex center) instead of constant x-axis values for all resulting flows, the positions for the DNS case are presented in Figure 10, they include the peak of k position that will be considered only in the k budget analysis. To establish the accuracy of each model's solution the average normalized error between the DNS and URANS profiles has been computed for each detection point and presented in Table 5. The velocity profiles are obtained with the sampling of N_p equally spaced points from the interpolated velocity profiles obtained for the different simulations (this process was implemented to account for the different cell distribution between the DNS and URANS simulations, the N_p values that have been considered are $N_p = 300, 500$ observing negligible differences across the two sets and confirming the result independence from the discretization), each position is indicated with the i index and the mean difference is computed with the following method:

$$\Delta U^j = \frac{\sum_{i=1}^{N_p} \left[(U_i^j - U_i^{DNS})/U_i^{DNS} \right]}{N_p}$$

Where ΔU^j represents the average velocity difference for the $j-th$ turbulence model, $j = KE,\ LSKE,\ KWSST,\ SARC$.

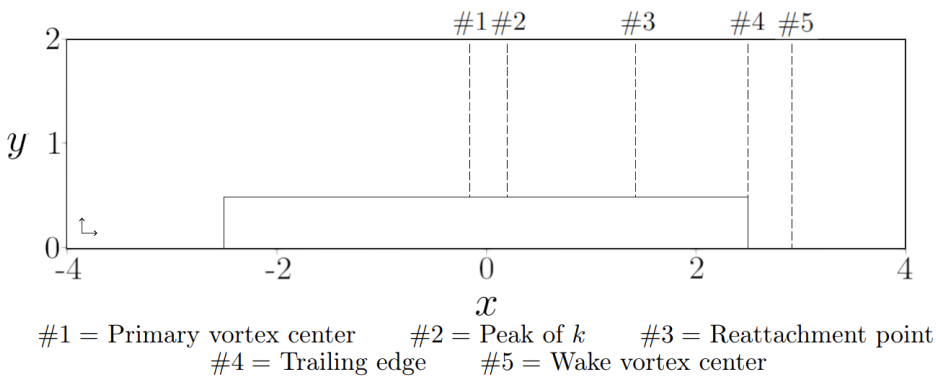

Figure 10: Velocity and budget of k terms measurements positions.

The LSKE and KWSST models are the best performer in the region of the primary vortex with an average velocity difference of -0.0197 and 0.0171. In the following two positions the LSKE model is the most accurate out of the four. In the rear part of the body, at the center of the wake vortex the SARC model outperforms the other two-equation models and achieves the smallest difference compared to the DNS, this result is in agreement with the comparison of the pressure coefficient over the backside of the cylinder in which this model is again the most accurate.

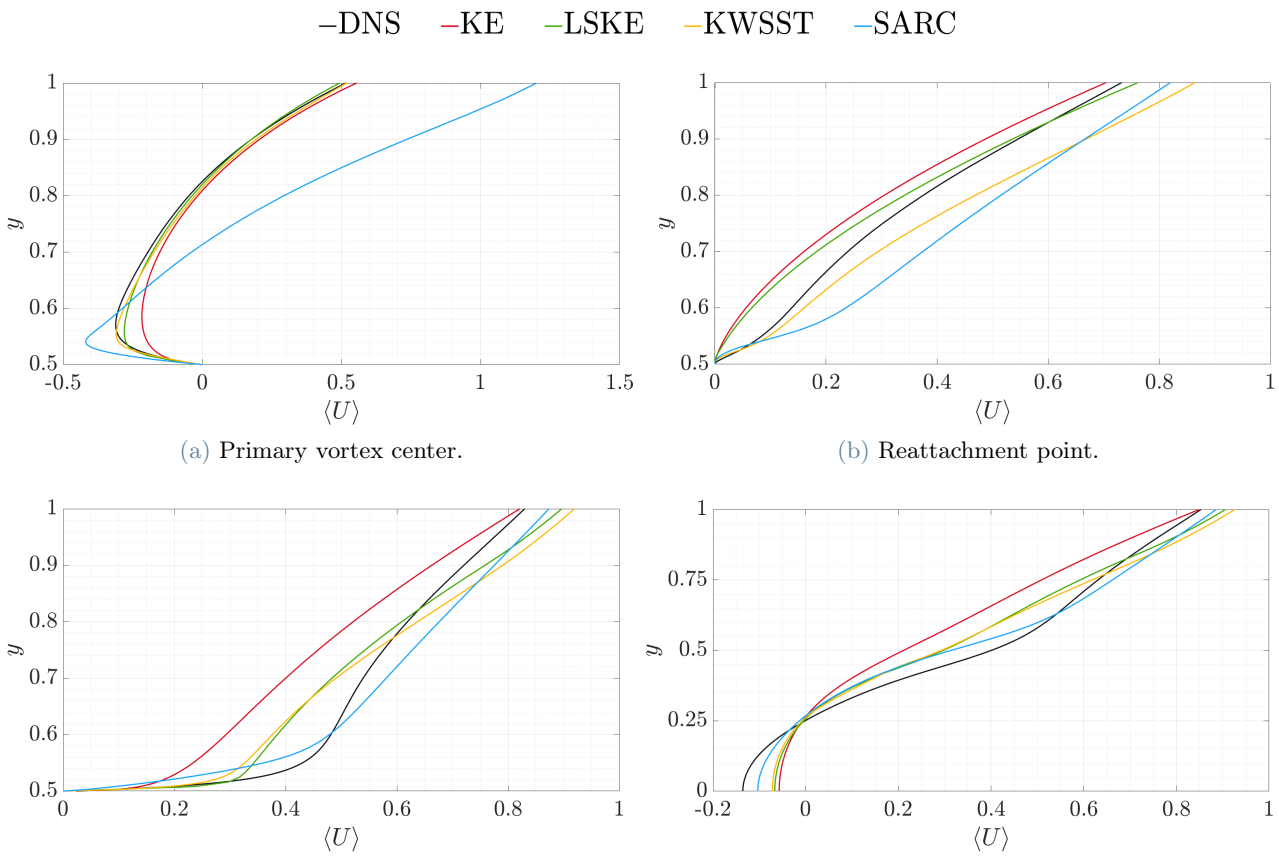

(a) Primary vortex center.

(b) Reattachment point.

(c) Trailing edge.

(d) Wake vortex center.

Figure 11: Velocity profiles at four topological point of interest.

Averaged velocity difference, ΔU^j				
	Primary v. center	Reattachment Point	Trailing edge	Wake v. center
KE	-0.0359	-0.0998	-0.0571	-0.1920
LSKE	-0.0197	-0.0663	-0.0007	-0.1191
KWSST	-0.0171	0.0733	0.0064	-0.1083
SARC	0.0990	0.1187	0.0118	-0.0933

Table 5

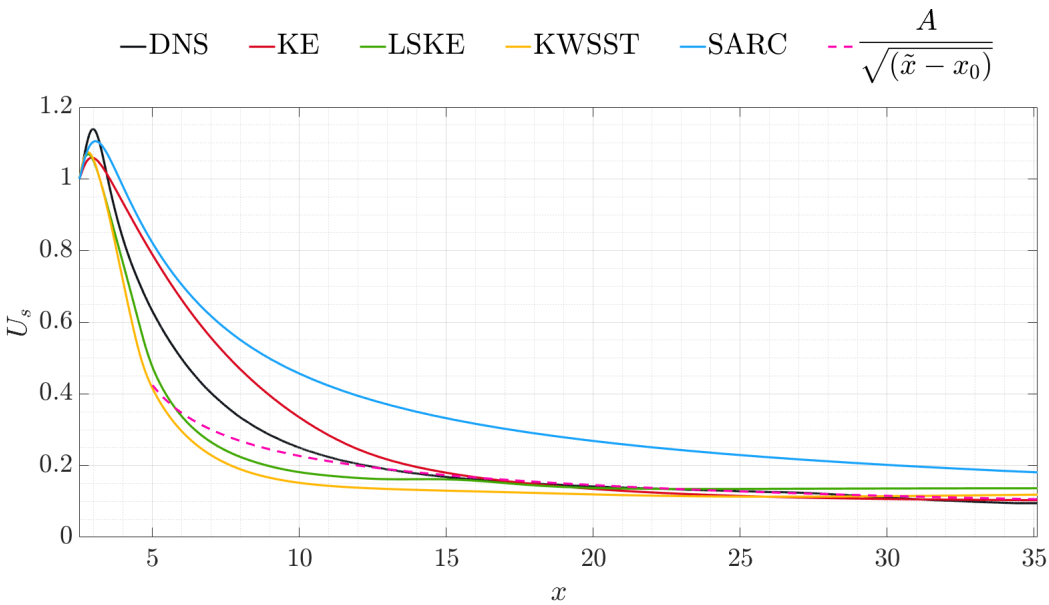

Figure 12: Velocity defect along the flow center-line at $y = 0$.

We now move to the far wake region. As detailed in Pope (2000), when moving far enough from the body surface the wake looses information about the geometry and reaches a self-similar velocity profile. In particular, the theory predicts that the velocity defect U_s at the center-line in the far wake decays as $x^{-1/2}$. With U_s defined as:

$$U_s(x) = U_c - \langle U(x, 0, 0)\rangle$$

Where U_c indicates the freestream velocity, $U_c = 1$ in this flow. The far wake region is identified as the region in which $U_s/U_c \to 0$ and in experiments the self similar behaviour that characterizes this region has been observed when the velocity ratio $U_s/U_c < \frac{1}{10}$. Additional variables need to be defined in order to evaluate the possible self similarity of the wakes predicted by the four turbulence models: the half width $y_{\frac{1}{2}}$ and the scaled velocity defect $f(\xi)$. The half width $y_{\frac{1}{2}}$ is defined such that:

$$\langle U(x, \pm y_{\frac{1}{2}}, 0)\rangle = U_c - \frac{1}{2}U_s(x)$$

And it defines the scaled cross-stream coordinate $\xi(x) = y/y_{\frac{1}{2}}$. The self similar velocity defect is computed as:

$$f(\xi) = [U_c - \langle U(x, y, 0)\rangle]/U_s$$

In Figure 12 the variation of the velocity defect at the center-line is presented for the DNS case and the four turbulence models, a fast decay of U_s is observed for all simulations in the near wake while in the far wake all the models tend asymptotically to the ratio $U_s/U_c \approx 1/10$. The rate of decay of the computed solutions can be evaluated with the comparison to the expected $x^{(-1/2)}$ rate indicated with the dotted red line, only the DNS solution presents the expected decay rate in the region $20 < x < 30$, the function utilized for this comparison is $\frac{A}{\sqrt{\tilde{x}-x_0}}$ with $A = 0.6$, $\tilde{x} = x - 2.5$ and $x_0 = 0.5$. To assess the self similarity of the wake velocity profiles obtained by the DNS solution and the four turbulence models in Figure 13 three positions are considered, $x = 12.5, 22.5$ and 32.5 that equate to a distance of $10D$, $20D$ and $30D$ from the cylinder. It is possible to observe, for all five cases, that although the predicted velocity defect profiles in the region $-1 < \xi < 1$ are self-similar, in the external part of the wake there are still differences between the scaled velocity defect profiles. Given these results and the rate of decay presented in Fig. 12 it possible to determine that a self similar behaviour has not yet been achieved by any of the simulations inside the domain with only the DNS solution approaching the expected decay rate of the velocity defect. The value of Us/U_c also indicates that the simulation domain considered is not large enough in the y direction to evaluate the far wake regions with only the DNS and KE solution achieving a velocity ratio U_s/U_c below $1/10$ at $x = 35$.

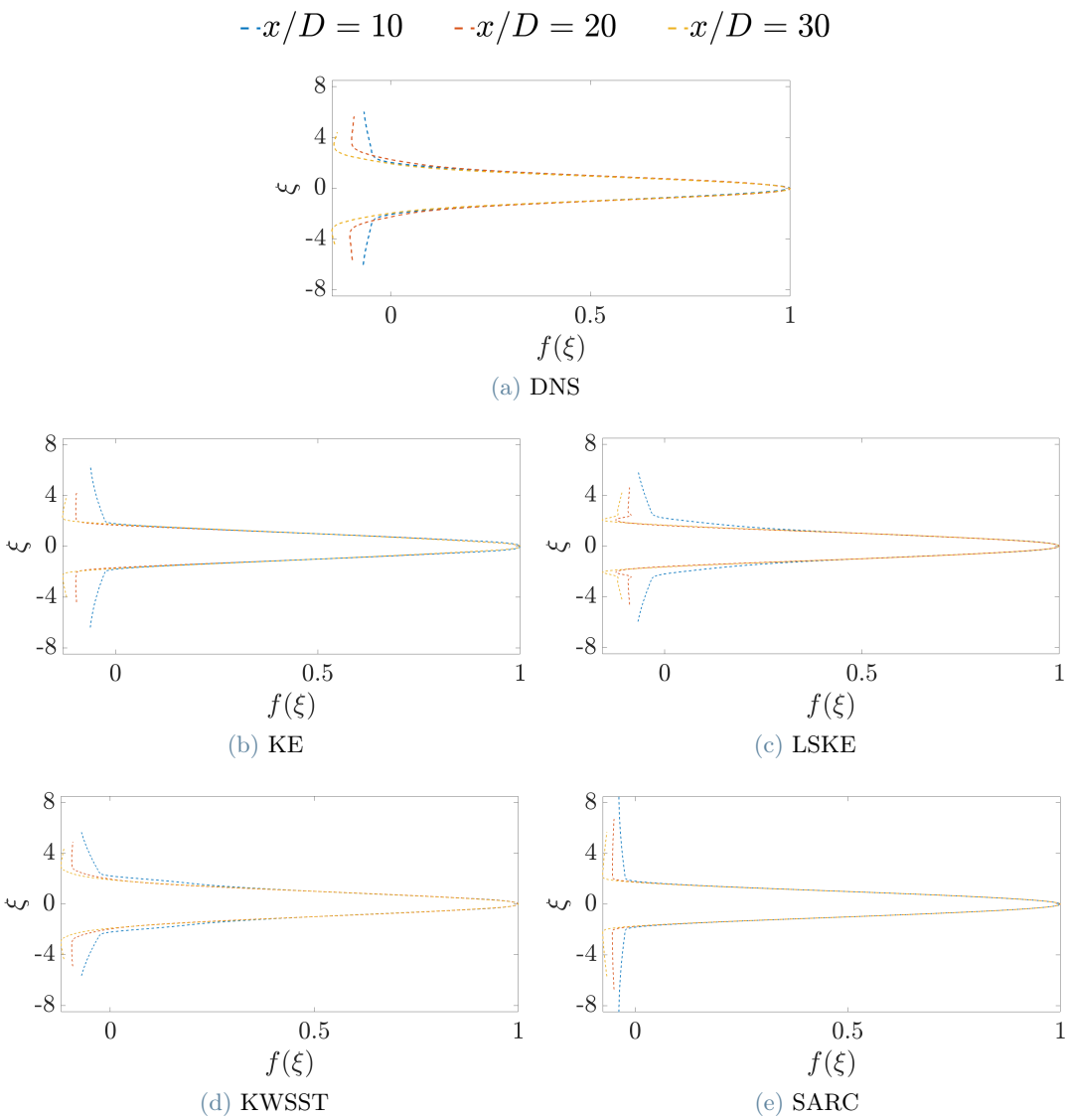

(a) DNS

(b) KE

(c) LSKE

(d) KWSST

(e) SARC

Figure 13: Scaled velocity defect at three positions for the DNS and URANS simulations.

3.3. Turbulence kinetic energy budget

The novelty introduced in this work is to assess the accuracy of the turbulence models by investigating the budget of the turbulent kinetic energy and specifically the different terms that contribute to it. Thanks to the detailed information obtained by the DNS it is possible, through the postprocess of the simulation data, to calculate exactly the value of the mean terms of the budget equation. The k equation considered is the following (Pope, 2000):

$$\frac{\mathrm{D}k}{\mathrm{D}t} = D + P - \epsilon \tag{4}$$

From left to right the terms presented are the total derivative of k, turbulent transport D, production P and dissipation ϵ.

To compare the different components of the TKE budget, only turbulence models that present a modelled equation for k need to be considered, i.e the KE, LSKE and KWSST models. For the SARC case this comparison is not possible as it is a one equation model for the viscosity $\tilde{\nu}$.

When considering the k transport equation applied to URANS simulations and the mentioned turbulence models it is important to notice that the total derivative and production terms are considered known while the dissipation and turbulent transport terms require modelling in order to solve the equation. An individual presentation of each budget terms for the URANS simulations is now provided, starting from the total derivative calculated as:

$$\frac{\mathrm{D}k}{\mathrm{D}t} = \frac{\partial k}{\partial t} + U \cdot \nabla k \tag{5}$$

The turbulent transport term is expressed as a function of the energy flux T':

$$D = -\nabla \cdot T' \tag{6}$$

$$T' = \frac{1}{2}\langle u_i u_j u_j \rangle + \frac{\langle u_i p' \rangle}{\rho} - 2\nu \langle u_j s_{ij} \rangle \tag{7}$$

The term $\nabla \cdot T'$, as previously indicated, cannot be computed given the information obtained by the solution of the URANS equations and modelled with the the gradient-diffusion hypothesis, obtaining:

$$D = \nabla \cdot (d \nabla k) \tag{8}$$

The production term for a 2D flow on the $x - y$ plane is the following:

$$P = -\langle uu \rangle \frac{\partial U}{\partial y} - \langle uv \rangle \left(\frac{\partial U}{\partial y} + \frac{\partial V}{\partial x} \right) - \langle vv \rangle \frac{\partial V}{\partial y} \tag{9}$$

In the URANS simulations only the mean components of velocity are evaluated, according to the turbulent viscosity hypothesis the production term is then calculated as a function of $\bar{S_{ij}}$:

$$P = 2\mu_t \bar{S_{ij}} \bar{S_{ij}} \geq 0 \tag{10}$$

$$\bar{S_{ij}} = \frac{1}{2} \left(\frac{\partial \langle U_i \rangle}{\partial x_j} + \frac{\partial \langle U_j \rangle}{\partial x_i} \right) \tag{11}$$

The dissipation rate is defined as:

$$\epsilon = 2\nu \langle s_{ij} s_{ij} \rangle \tag{12}$$

$$s_{ij} = \frac{1}{2} \left(\frac{\partial u_i}{\partial x_j} + \frac{\partial u_j}{\partial x_i} \right) \tag{13}$$

However, in the case of the two-equations turbulence models considered, this term can be obtained from the modelled equation for ϵ (KE and LSKE) or ω (KWSST).
The first analysis regards the turbulent kinetic energy distribution in the flow field. In the reference solution this quantity assumes values close to zero up to $x < -1.3$, after this point the sharp increase of k indicates a rapid change of the flow and corresponds to the transition of the laminar shear layers, the peak of k is then achieved inside the primary vortex. Looking over to the URANS simulations, presented in Fig 14, the KE model and the KWSST model show similar results in the region around the first half of the cylinder. Both of them fail to capture the large laminar portion of the flow after the interaction with the leading edges of the cylinder, this is indicated by the regions of $k \neq 0$ that extend along the shear layer from the primary vortex towards the upstream edges. The concentration of k from the LE indicates that the shear layer transition and the formation of turbulent structures predicted by these two models do not occur at $x > -2$ but right after the interaction with the LE corners, as it will be confirmed by the analysis of the production term. Out of the two, the KWSST model is more accurate when considering the position of the peak k value (presented in Table 6). The LSKE model presents a different solution, in the stagnation region an unexpected value of $k > 0$ is observed. The overprediction of the turbulent kinetic energy is a well known phenomena described by Durbin Durbin (1996) as the stagnation point anomaly and, as suggested by the name, regards impinging flows presenting regions of $U, V \approx 0$. The reason behind this inaccuracy is the increase of the turbulent time scale T (e.g k/ϵ) and the effect that it has on the turbulent viscosity, calculated as $\nu_t = CkT$. This large value of T introduced into the ϵ equation leads to a very small value of dissipation in the stagnation region, that allows for an inaccurate and spurious high value of k. This miscalculation may then affect the region surrounding the stagnation point leading to an overprediction of k around the LE corners. After this initial region the model predicts lower values of k along the shear layer compared to the other two models. A second region of high turbulent kinetic energy is the primary vortex, this model is the most accurate in predicting the peak value of k, that is located in this region, however the position indicated is further downstream by $0.475D$ with respect to the DNS. The turbulent kinetic energy profiles obtained along the y direction are presented in Figure 15, similarly to the approach used in the comparison of the velocity profiles, they have been obtained at the position of key flow features (Primary vortex center, reattachment point, peak of turbulent kinetic energy, trailing edge and secondary vortex center) and thus at different x-axis coordinates for each turbulence model. Along the lateral side of the body as can be observed in Figure 15a-15c-15b the LSKE models is the most accurate compared to the DNS results, especially in the region close to the cylinder. However it can be observed that all three models underestimate the value of mean k at the primary vortex and at the peak of k positions. Focusing on the trailing edge, the KE and LSKE models perform better than the KWSST one, predicting higher values of k. Moving to the wake all three models fail to mimic the DNS profile especially around $y = 0$ where the standard KE and KWSST largely

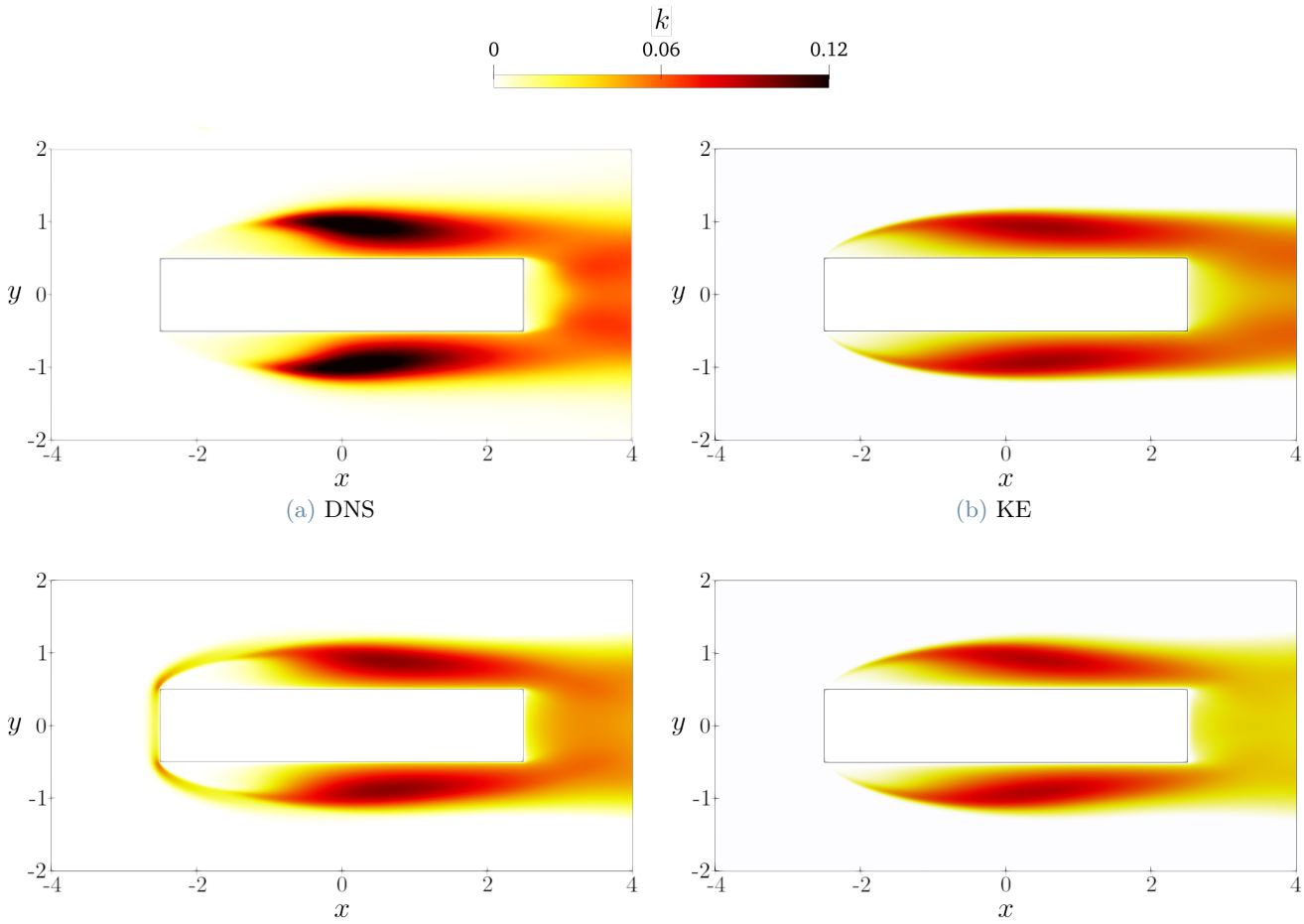

(a) DNS (b) KE

(c) LSKE (d) KWSST

Figure 14: Colourmap of the mean turbulent kinetic energy.

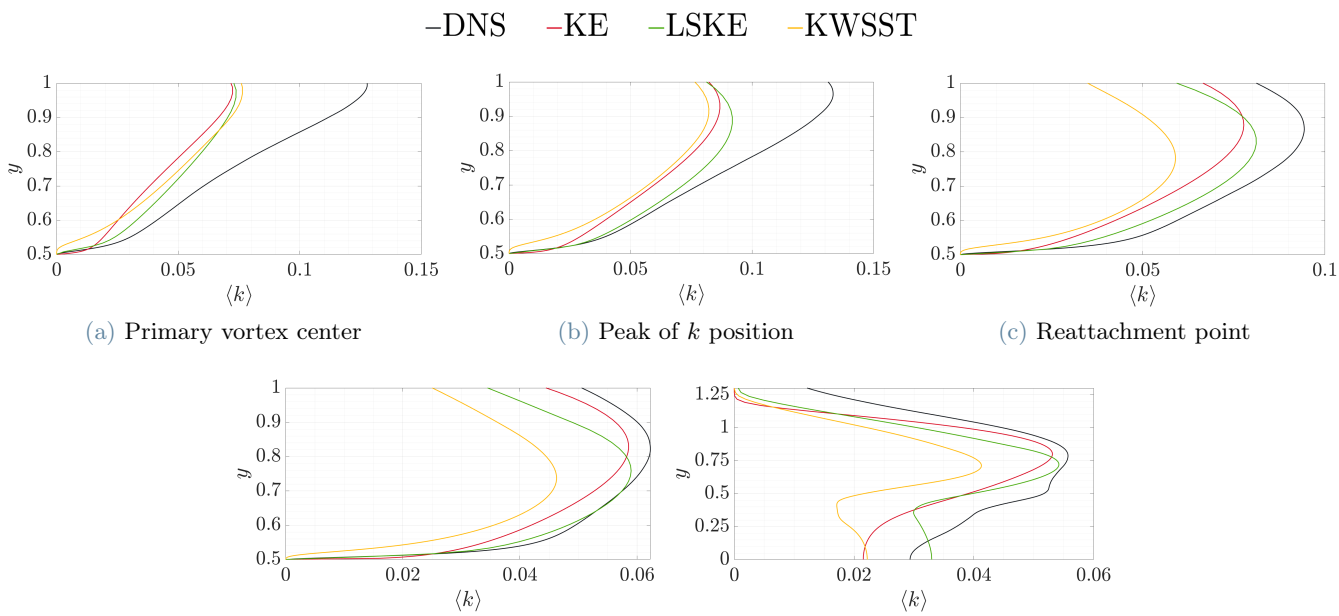

(a) Primary vortex center (b) Peak of k position (c) Reattachment point

(d) Trailing edge (e) Wake vortex center

Figure 15: Mean k profiles.

		DNS	KE	LSKE	KWSST
$\boldsymbol{k}$	k_{max}	0.135	0.0867	0.092	0.0824
	(x_m, y_m)	$(0.15, 0.98)$	$(0.475, 0.929)$	$(0.625, 0.888)$	$(0.418, 0.914)$
$\boldsymbol{\epsilon}$	ϵ_{max}	0.189	0.0954	0.0794	0.0885
	(x_m, y_m)	$(2.5, 0.5)$	$(-1.734, 0.885)$	$(-2.496, 0.551)$	$(-1.483, 0.944)$

Table 6: Turbulent kinetic energy and dissipation peak positions.

	DNS	KE	KELS	KWSST
Primary v. center	0.1899	0.1202	0.1016	0.0961
Peak of k position	0.1515	0.0883	0.0859	0.752
Reattachment point	0.0613	0.0570	0.0579	0.0356
Trailing edge	0.0300	0.0920	0.0260	0.0208
Wake v. center	0.0330	0.0221	0.0233	0.0194

Table 7: Maximum value of k observed at each investigated position.

underestimate the value of k, in the region for $0.5 < y < 1$ the KE and LSKE models are more accurate in the prediction of the maximum value of k and of its position. The underestimation of the mean turbulence kinetic energy, especially in the first and second positions is a direct consequence of the inaccurate distribution of k in the URANS simulations. While in the DNS case the primary vortex presents a sudden increase k due to the shear layer transition, in the URANS simulations the early transition leads to a larger turbulent region and consequently lower peak values of k.

Moving over to the budget terms analysis, the first to be considered is the production as it describes the transfer of energy from the mean flow to the fluctuating velocity field. The production mechanism and the components contributing to the total production value are described accurately in Chiarini & Quadrio (2021). In the reference study (Figure 16a) P is nearly zero up to $x = -2$, after this point the instability of shear layer and the consequent formation of the KH vortices in a region of consistent mean flow gradients leads to the transfer of energy from the mean flow to streamwise velocity fluctuations and an increase of k. This transition region and the primary vortex are the regions with the strongest P value. A second region characterized by a conspicuous value of P is identified in the wake of the body, along the separation line that detaches from the TE. As previously mentioned a small region of negative production can be identified near the cylinder lateral walls towards the leading edges.

The comparison of the URANS results indicates that none of the models implemented accurately predicts the large region of near zero production for $x < -2$. For the KE and KWSST model non-null values of P are observed along the shear layer, starting in proximity to the LE corners, inside the primary vortex region and with lower intensity in the wake region. These results indicate that the simulated laminar/turbulent transition in the URANS mean flow fields occurs upstream than experienced by the DNS, leading to the distribution of k analyzed previously and the formation of a large turbulent region along the cylinder. For the LSKE model the production is concentrated in the region adjacent the first square corners and in the primary vortex, clearly the peak of production near the LE indicates a weakness of the model in the prediction of the flow interaction with sharp corners after the stagnation region. The turbulent kinetic energy production profiles presented in Figure 17 show that at the primary vortex center and at the peak of k positions all three models underestimate the production value. In Tab. 7 the maximum values achieved by this term at each position are summarized, with the standard KE and LSKE models offering a superior performance over the KWSST one. At the second location similar results are observed. It should be also noted that the value presented for the KE model at the reattachment point is affected by the large over-prediction of P near the wall by the model that is correctly dumped in the LSKE variant.

The bulk of the production for all the URANS simulation occurs upstream compared to the DNS reference leading to the results in Figure 17a-17b. In Fig. 17c-17b is shown how the DNS simulation predicts a negative value of production near the wall that is not captured by any of the turbulence models given the impossibility for these models to predict $P < 0$. In the wake region (Fig. 17e) the DNS profile is characterized by two local peaks, the highest is placed closer to the body centerline and corresponds to the production associated with the rear recirculating region shear layer while the lower one is the effect of the primary vortex production. All three models are inaccurate in the prediction of these peaks, the maximum production values are lower than the reference one and compared to the DNS maximum production that occurs at $y = 0.46$, are placed further away from cylinder body at $y = 0.892$ for KE, $y = 0.782$ for LSKE and $y = 0.724$ for KWSST. It can be suggested

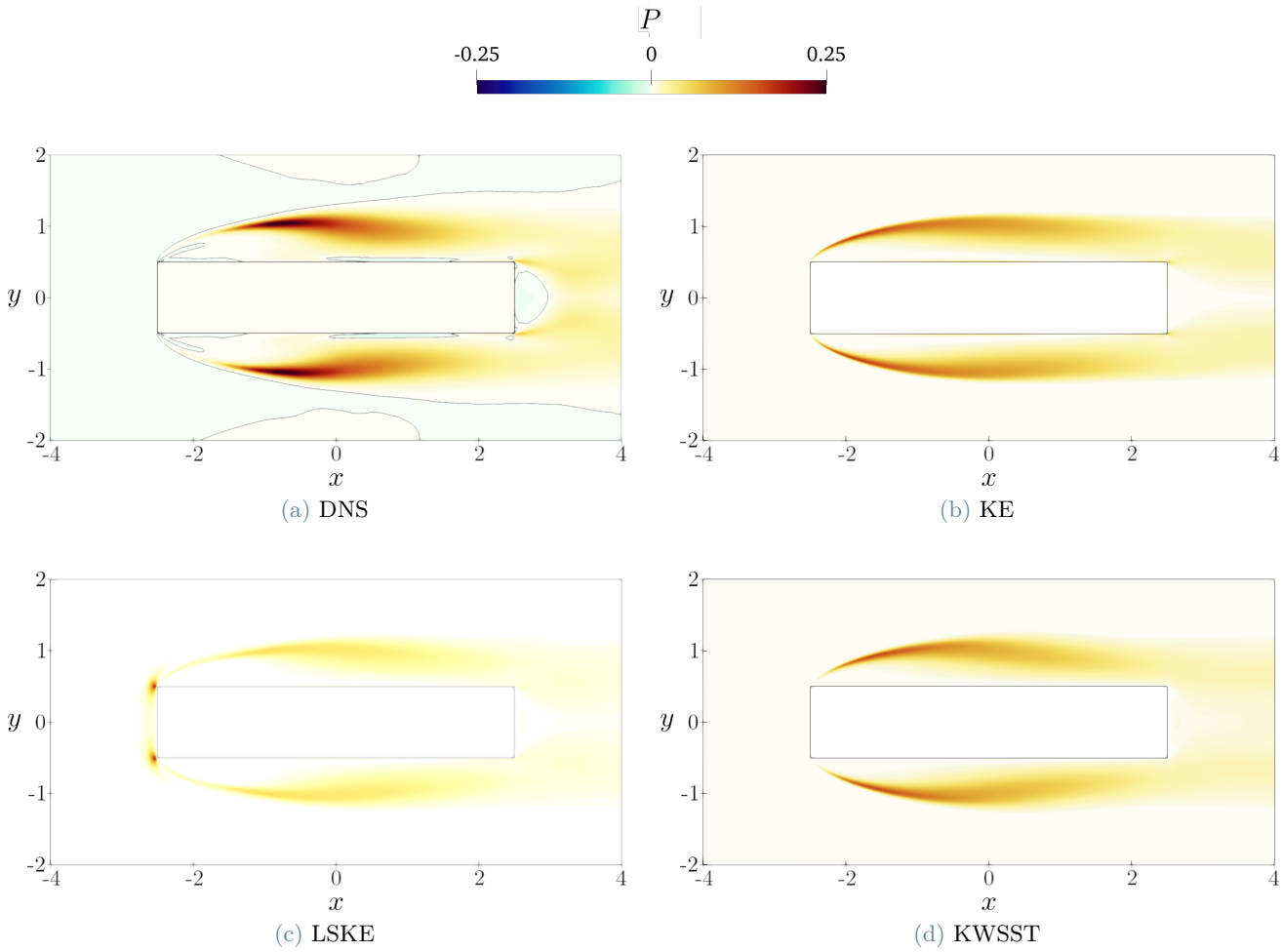

Figure 16: Colourmap of the mean kinetic energy production term, P. In (a) the black contour lines denote $P = 0$

that these values represent the production of k associated with the primary vortex. Only the Launder Sharma model predicts a consistent increase in production connected to wake vortex shear layer with a local maximum at $y = 0.482$, the position of the peak is quite accurate while the value is much smaller than the DNS one.
The second budget term analyzed is the mean dissipation of k. The reference flow in Figure 18a shows a region of strong dissipation that extends from the shear layer at $x \approx -1.5$ to the primary vortex core. As described in Chiarini & Quadrio (2021) in this region the main contributions comes from the streamwise and spanwise components $\langle uu \rangle$ and $\langle ww \rangle$. Strong dissipation is also found close to the wall, with the peak value around the trailing edge corners (Table 6), in this region the viscous effects are dominant and the flow behaviour in the near wall region is comparable to a standard channel flow with an adverse pressure gradient. For the URANS simulations the erroneous prediction of the shear layer behaviour leads, in the case of KE and KWSST to non null values of dissipation starting form the LE corners, this phenomena is connected to the early transition presented in the production term analysis. The development of turbulent structures along the shear layer and a large fully turbulent region lead to a larger area of $\epsilon \neq 0$. The LSKE model predicts correctly the presence of a region of strong dissipation in the primary vortex but due to its shortcomings in describing the flow around the leading edges the dissipation peak is located around these areas. To evaluate the difference between the dissipation obtained from the URANS simulation and the DNS results at the specific topological points of interest previously introduced, the average difference of the dissipation profiles has been computed in a similar fashion to the velocity profile comparison presented in Section 3.2 (Table 8). It can be observed that all three turbulence models perform similarly and are quite accurate in the region away from the wall but all of them fail to represent the intense dissipation occurring at the wall. To quantify this difference the average mean dissipation is calculated over a line parallel to the cylinder longitudinal side and placed at $y = 0.015$. This distance of $0.015D$ is considered to evaluate the physical value obtained from the simulation while the value of dissipation calculated from the first cell next to the wall would be affected by the $\epsilon = 0$ boundary condition implemented. The results are: 0.0206 for the DNS, 0.0107 for KE, 0.0120 for LSKE and 0.0098 for KWSST. A strong under-prediction of this value can be noted for all models with the LSKE model being slightly more

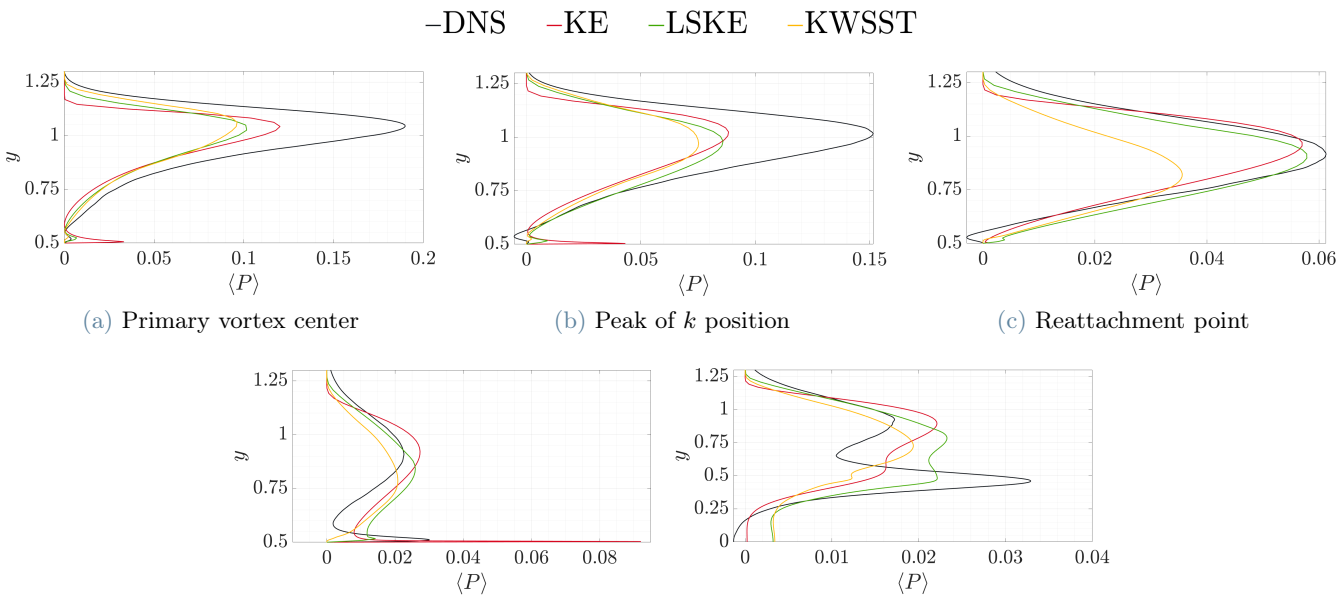

(a) Primary vortex center (b) Peak of k position (c) Reattachment point

(d) Trailing edge (e) Wake vortex center

Figure 17: Mean production of k profiles.

Averaged ϵ difference					
	Primary v. center	Peak of k	Reattachment Point	Trailing edge	Wake v. center
KE	-0.0045	-0.0058	-0.0026	-7.00×10^{-4}	-0.0018
LSKE	-0.0043	-0.0047	-0.0018	-5.62×10^{-4}	-4.94×10^{-4}
KWSST	-0.0028	-0.0045	-0.0047	-0.0014	-0.0020

Table 8: Average dissipation difference between URANS and DNS results at different topological points of interest.

accurate than the other options. Examining the wake region results the turbulence models tend to underestimate the dissipation inside the recirculating region and overestimate it further away from the cylinder (Fig. 19e). While the DNS profile is characterized by a region of fairly constant dissipation of $\epsilon^{DNS} \approx 0.016$ the three turbulence models have well defined peaks resulting from the high dissipation region originating from primary vortex and that extends after the trailing edge.
From the DNS reference solution it is possible to observe that a significant role in the dissipation of k is played by the spanwise contribution (Chiarini & Quadrio, 2021), in this study only 2D URANS simulations are considered thus limiting the ability to describe all the span-wise phenomena and and possibly leading to the underprediction of the dissipation value that in this case accounts only for stream wise and cross stream contributions.

Average mean Dk/Dt difference					
	P. Vortex center	Peak of k	Reattachment Point	Trailing edge	W. vortex center
KE	-0.0186	-0.0224	-0.0155	-0.0098	-0.0077
LSKE	-0.0190	-0.0235	-0.0152	-0.0106	-0.0081
KWSST	-0.0189	-0.0218	-0.0171	-0.0110	-0.0074

Table 9: Average Dk/Dt difference between URANS and DNS results at different topological points of interest.

Comparing the total derivative terms of the turbulent kinetic energy equation we can observe that the KE and KWSST models correctly identify the total derivatives distribution in the region between $-2.5 < x < -1$, characterized by an inner slightly negative layer surrounded by a positive one. The LSKE model case predicts instead an incorrect region of strong total derivatives, both positive and negative, around the LE square corners, indicating again its limits in modelling the interaction with sharp corners. The average differences for this parameter compared to the reference DNS are presented in Table 9, all models perform similarly in the points of interest and no model is able to clearly outperform the others. Similar considerations can be done for the

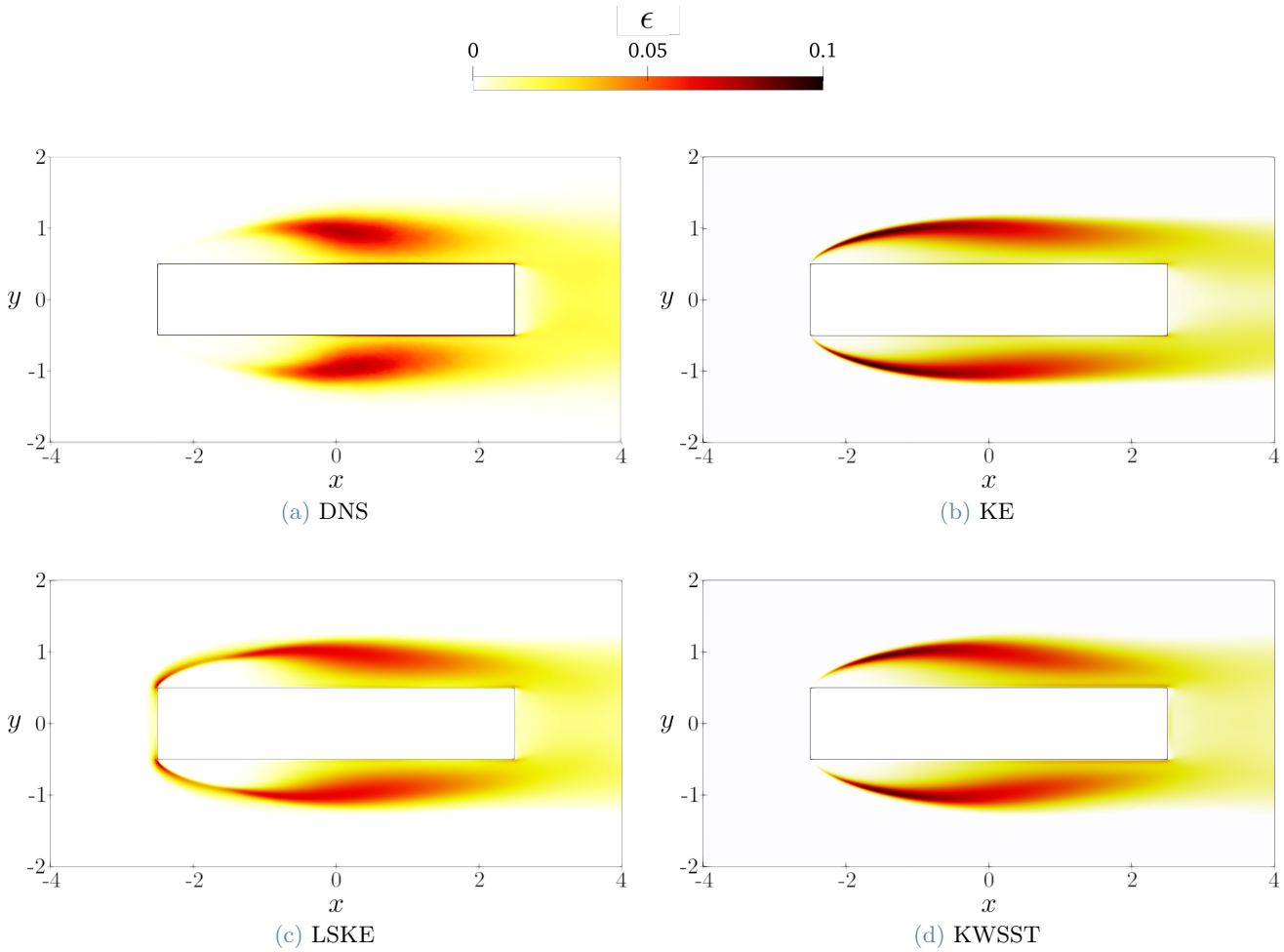

(a) DNS (b) KE

(c) LSKE (d) KWSST

Figure 18: Colourmap of the mean turbulent kinetic energy dissipation, ϵ.

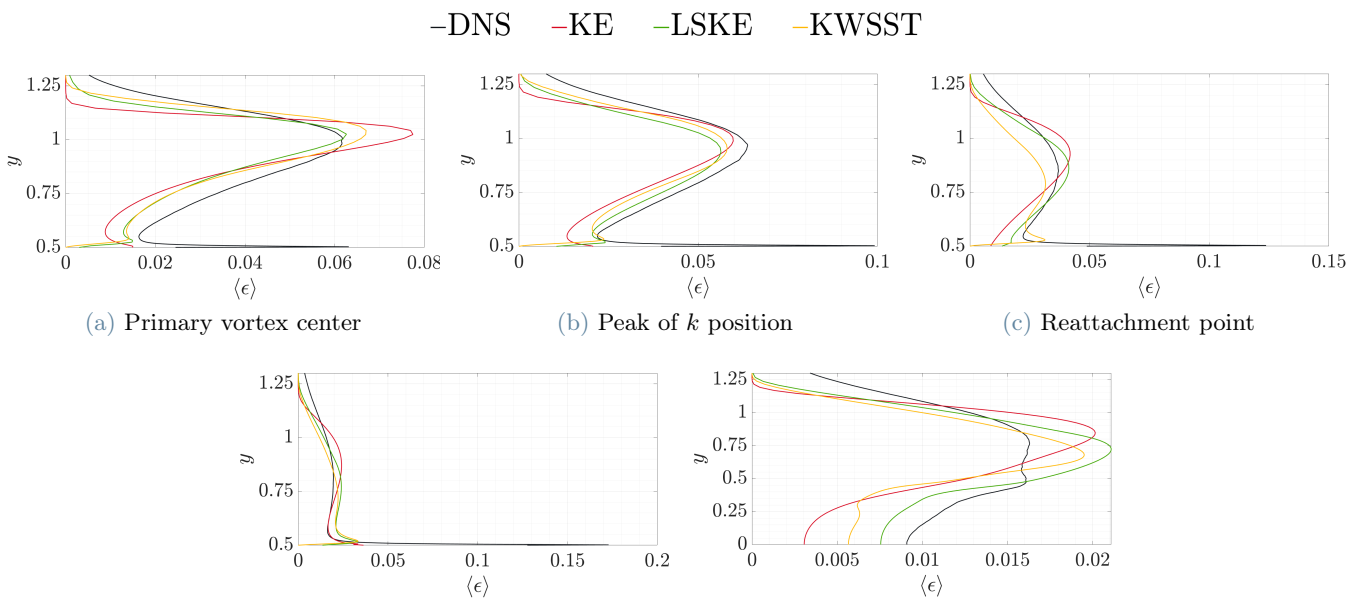

(a) Primary vortex center (b) Peak of k position (c) Reattachment point

(d) Trailing edge (e) Wake vortex center

Figure 19: Mean dissipation of k profiles.

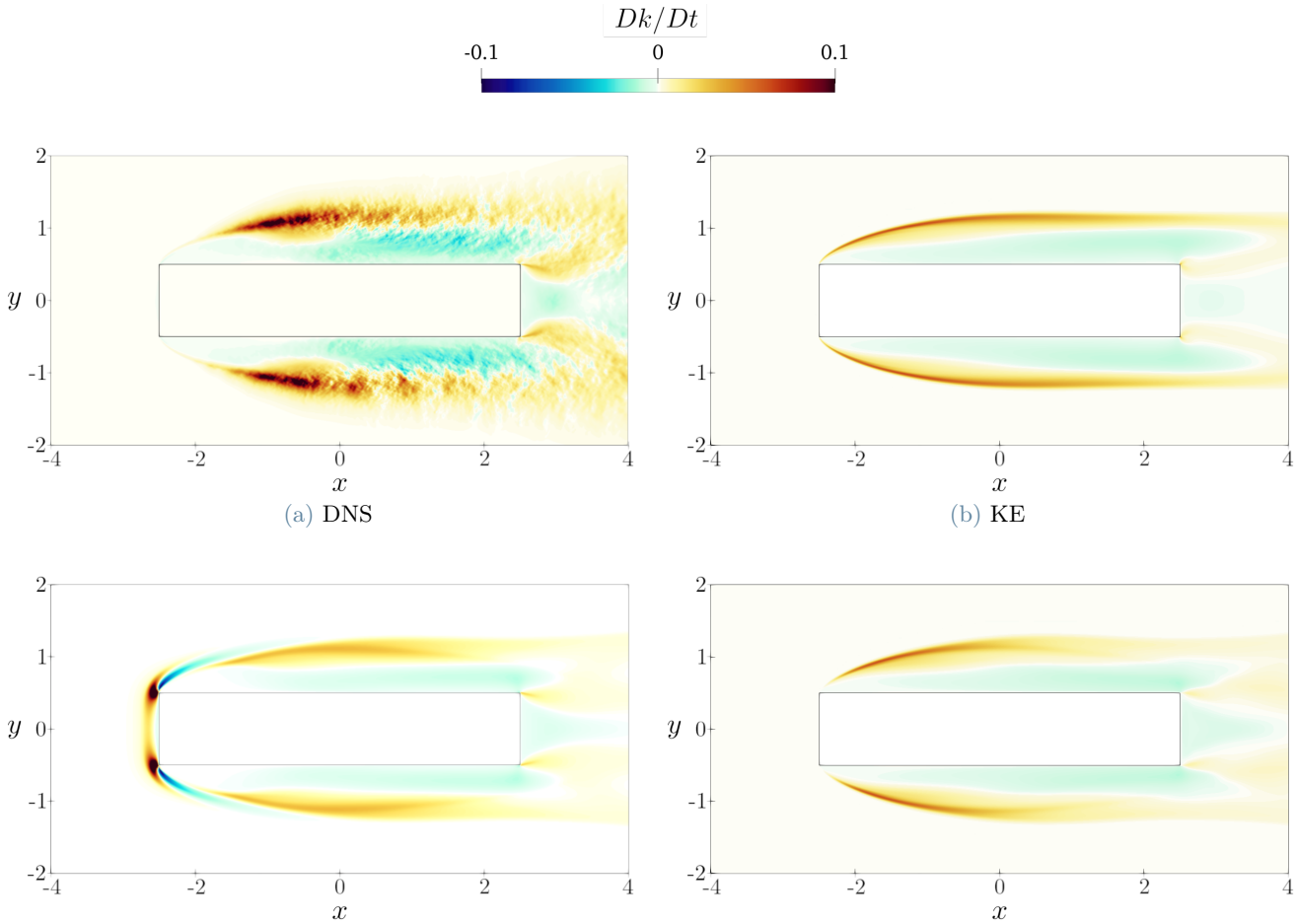

(a) DNS (b) KE

(c) LSKE (d) KWSST

Figure 20: Colourmap of the mean turbulent kinetic energy total derivative, $\frac{\mathrm{D}k}{\mathrm{D}t}$

.

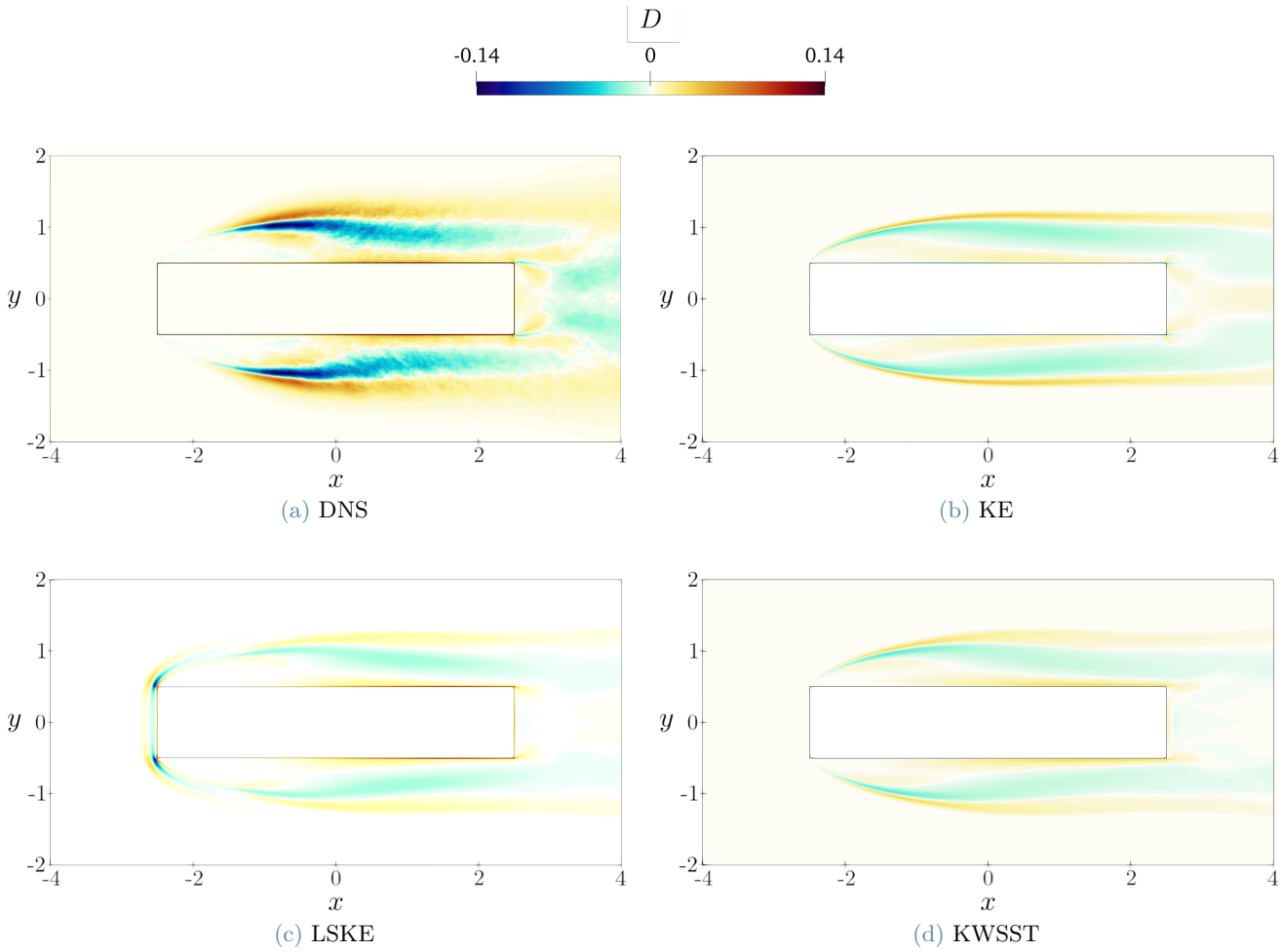

(a) DNS (b) KE

(c) LSKE (d) KWSST

Figure 21: Colour map of the mean turbulent kinetic energy diffusion D.

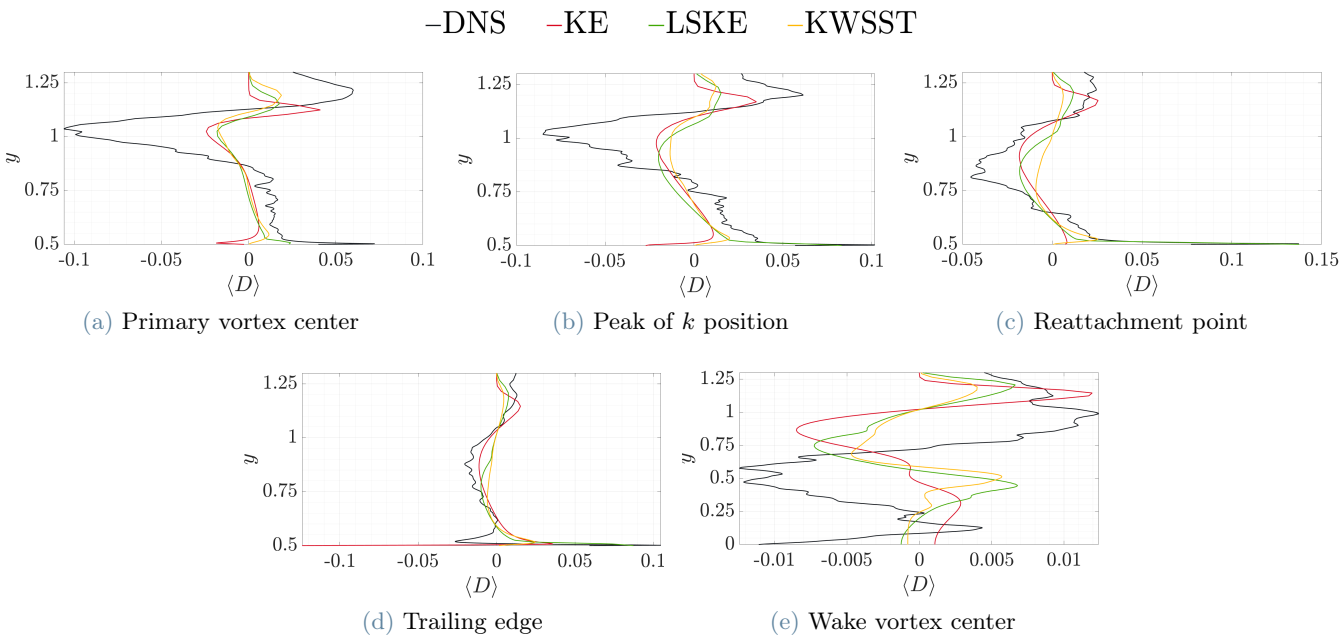

(a) Primary vortex center (b) Peak of k position (c) Reattachment point

(d) Trailing edge (e) Wake vortex center

Figure 22: Mean diffusion of k profiles.

D difference					
	P. Vortex center	Peak of k	Reattachment Point	Trailing edge	S. vortex center
KE	-4.41×10^{-4}	0.0010	-9.30×10^{-4}	2.98×10^{-5}	-8.88×10^{-4}
LSKE	-3.38×10^{-4}	-2.75×10^{-4}	-1.48×10^{-4}	4.40×10^{-4}	-8.87×10^{-4}
KWSST	-5.64×10^{-4}	-1.14×10^{-4}	2.02×10^{-4}	3.29×10^{-4}	-9.60×10^{-4}

Table 10: Average diffusion difference between URANS and DNS results at different topological points of interest.

diffusion term, all models can identify the three defined regions of positive and negative diffusion along the cylinder with sufficient accuracy. One critical feature of the DNS result is a strong positive diffusion near the body walls in the region $0 < x < 2.5$ that all models are able to identify, however the KWSST and KE models tend to underpredict its value, as observed in Figure 22a-22c-22b. The LSKE model shows again an erroneous behaviour in the region before the leading edges with both strong and negative diffusion. A region of negative diffusion can be observed in the wake of the body in the DNS results but none of the turbulence models are able to correctly predict it, all the models fail to identify the position and the intensities of the positive and negative peaks of diffusion in the wake (Fig. 22e).

In light of the results presented in Section 3.2 and 3.3 a few considerations can be made regarding the choice of a turbulence model when dealing with bluff body flows. As already indicated in Mannini *et al.* (2010) and Patruno *et al.* (2016) URANS simulations are unable to describe the complex structure of this type of flow at a low Re condition, the laminar shear layer proves to be the most challenging aspect of this configuration with both the KWSST and KE models that are unable to predict the laminar separation and the correct position of the transition. The LSKE model appears to be in most comparisons the most accurate out of the three two-equations models. It is the only one partially capable of accounting for the complexity of the main recirculating region, predicting a teardrop shaped main vortex that more accurately resembles the DNS solution. Analyzing the mean flow and the velocity profiles it returns more valid results compared to the the KE and KWSST models, being outperformed only by the SARC solution in the rear region of the cylinder. The weakness of this model is the description of the stagnation region and the interaction with the LE corners, a specific correction to this behaviour could improve even more its performance. Aside from this problem, and how it affects the region near the leading edge, the LSKE model seems to be the only one capable of capturing the behaviour the laminar shear layer and thus predict the rapid increase of TKE production at the transition location with consequently a slightly more accurate prediction of the kinetic energy values in the primary vortex and in the rest of the flow field.

3.4. Inflow condition effects

The effect of inflow turbulence intensity has been the subject of multiple studies, i.e.: Shirato *et al.* (2010); Ricci *et al.* (2017); Mannini *et al.* (2017). It has been noted that the increase of this parameter leads to a reduction of the recirculating region size, with effect on the pressure distribution and time average drag coefficient. In this section the effect of different incoming turbulence intensities in URANS simulations will be investigated considering two different flow conditions.

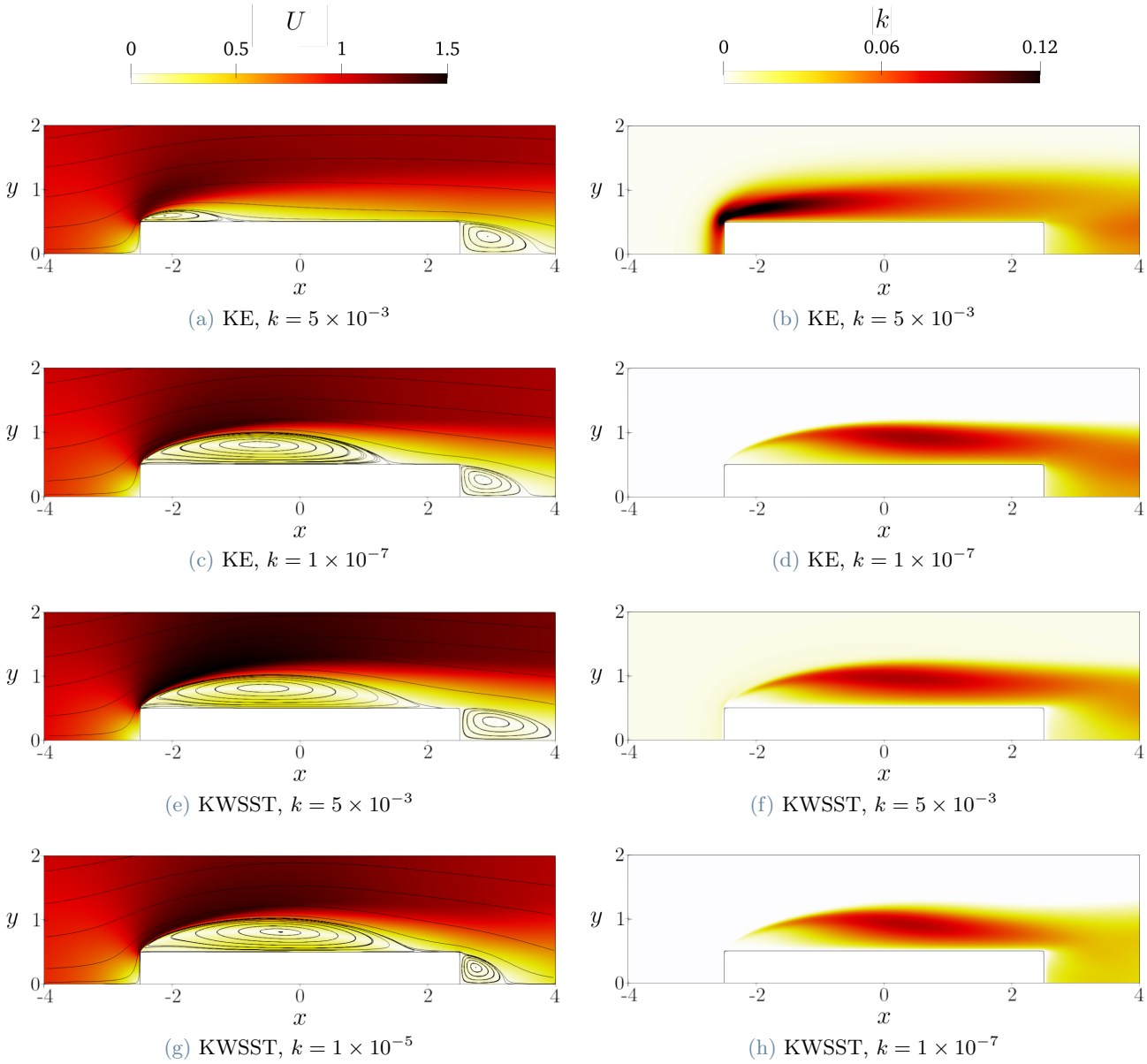

(a) KE, $k = 5 \times 10^{-3}$ (b) KE, $k = 5 \times 10^{-3}$

(c) KE, $k = 1 \times 10^{-7}$ (d) KE, $k = 1 \times 10^{-7}$

(e) KWSST, $k = 5 \times 10^{-3}$ (f) KWSST, $k = 5 \times 10^{-3}$

(g) KWSST, $k = 1 \times 10^{-5}$ (h) KWSST, $k = 1 \times 10^{-7}$

Figure 23: Comparison of the velocity and k colour map for the KE and KWSST model at two levels of inlet turbulent intensity.

.

In the OpenFOAM environment the control over the inflow characteristics is implemented with the selection of the dissipation ϵ and turbulent kinetic energy k at the inlet and farfield boundaries (Table 2). Two values of imposed k have been considered to evaluate the model dependence on inflow condition and they are $k = 1 \times 10^{-7}$ and $k = 5 \times 10^{-3}$ that equate respectively to a turbulence intensity of $2.58 \times 10^{-4}\%$ and 5.7% and are investigated with the standard KE and KWSST models.

The zero turbulence inflow condition has already been discussed in Sections 3.1-3.2-3.3, in this case the imposition of a boundary kinetic energy value of $k = 1 \times 10^{-7}$ instead of simply $k = 0$ is preferred to avoid stability issues with the OpenFOAM software. The second condition represents the case for a small turbulence intensity at the inlet. The results obtained by this flow condition are presented in Table 11 and differ noticeably from those in the zero turbulence case. For the KE model the main difference consists in the steady nature

	Inlet k	f	$\langle C_l \rangle$	$(C_l)_{rms}$	$(C_l)_{extremes}$	$\langle C_d \rangle$
KE	1×10^{-7}	0.0907	1.79×10^{-4}	0.165	± 0.235	0.931
	5×10^{-3}	-	1.35×10^{-8}	7.51×10^{-7}	$(+0.13, -0.139) \times 10^{-5}$	1.134
KWSST	1×10^{-7}	0.1099	1.33×10^{-3}	0.856	± 1.208	1.045
	5×10^{-3}	0.095	1.08×10^{-4}	1.004×10^{-3}	$(+1.25, -1.59) \times 10^{-3}$	0.921

Table 11: Comparison of the time averaged flow characteristics at different turbulent inlet conditions.

of the flow with a much smaller recirculating region on the side of the cylinder. The primary vortex extends for $-2.5 < x < -1.05$ with a noticeable reduction in length, $L_1 = 1.45$, compared to the zero turbulence case (Table 4). The wake vortex, that extends for $2.5 < x < 3.69$, remains similar to the previous case, suggesting a lower dependence from turbulence intensity of the near wake features, obviously given the steadiness of the solution no release of vortices appears after the cylinder. Looking at the TKE presented in Figure 23 it can be clearly observed how the interaction of the flow with the the LE square corners leads to high values of both production and dissipation in the cells immediately adjacent the corners. This behaviour has been previously encountered by Rodi (1997) in which the author suggests that the kinetic energy is extracted from the mean flow and transferred to the turbulent motions and dissipated, leading to the suppression of the mean flow phenomena such as the vortex shedding and the development of a large primary recirculating region.
For the KWSST model the results are quite different, the predicted flow is unsteady with a definite oscillation frequency of the C_l and C_d coefficients with a considerably smaller amplitude compared to the results presented in Section 3.2 as indicated by the $(C_l)_{rms}$ value and the $(C_l)_{extremes}$. Differently from the results obtained from the KE case and the results available in literature the primary and secondary recirculating regions extend more than in the zero turbulence case with the respective lengths of $L_1 = 4.77$ and $L_3 = 1.57$. These results indicate that the KWSST model is not accurate in the description of different flow condition with results that differ from similar experimental and numerical analysis.

3.5. Re=3x10^5 comparison

In order to evaluate the dependence on Reynolds number of the simulations the BARC flow at $Re = 3 \cdot 10^5$ has been simulated with the KE and KWSST models.
Compared to the flow at $Re_D = 3000$ both models shows a similar mean flow field with only the primary and wake vortices being predicted. For the KE model the primary recirculating bubble in the high Re case is more elongated with a value of $L_1 = 4.10$, longer by 0.18 units than the low Re case. The wake vortex length is slightly shortened by only 0.14 units, with $L_3 = 0.911$. The KWSST model on the other hand predicts a shorter primary and wake vortices ($L_1 = 4.26$, $L_3 = 0.704$).
The c_p plots are very similar for the two Reynolds numbers, the value $\langle c_p \rangle$ in the front region of the body is affected by the low pressure region induced by the primary vortex while downstream the pressure recovery after the reattachment leads to an increase of the coefficient. The $\langle c_f \rangle$ value along the lateral side is very different to the low Reynolds case, it is nearly constant with a minimum of -0.004 at $x = -0.18$ and a maximum of 0.003 at the trailing edge for the KE, a similar result is obtained by KWSST with $-0.0022 < \langle c_p \rangle < 0.0029$. These results indicate that the average flow velocity variation near the wall in the direction perpendicular to the wall is small, it is possible to suppose that a region of very slow flow is induced by the large main vortex. The TKE distribution (Fig. 24) in the flow field is similar to the low Reynolds URANS case, with strong values in the shear layer and in the primary vortex. These results indicate that the flow transition happens right after the LE corners, and is in line with the studies by Bruno *et al.* (2008); Zhang & Xu (2020); Crivellini *et al.* (2022). The increase of the Reynolds number induces an upstream shift of the position at which the KH vortices are generated, thus reducing or eliminating the laminar shear layer region. The effect of the increase in Re number to the vortex shedding of geometries with sharp corners was also presented by Sasaki & Kiya (1991), in which it is possible to observe experimentally the change in roll up position of the shear layer with the increase of Re. The three studies presented, that focus specifically on the BARC flow were obtained with LES at $Re_D = 4 \times 10^4$ while this present analysis regards the flow at $Re_D = 3 \times 10^5$, it would be reasonable to suppose that the same Re number effect on the shear layer transition is captured by the URANS simulations at even higher Re. This result indicates that, although incapable of predicting the secondary vortex, turbulence models and URANS simulations are more accurate in the description of high Re bluff body flows, compared to low Re cases.

	Re_D	f	$\langle C_l \rangle$	$(C_l)_{rms}$	$(C_l)_{extremes}$	$\langle C_d \rangle$
KE	3×10^3	0.0907	1.79×10^{-4}	0.165	± 0.235	0.931
	3×10^5	0.0859	6.18×10^{-4}	0.178	± 0.251	0.993
KWSST	3×10^3	0.1099	1.33×10^{-3}	0.856	± 1.208	1.045
	3×10^5	0.0953	-2.78×10^{-4}	0.864	$(+1.219, -1.220)$	1.122

Table 12: Comparison of the time averaged flow characteristics at different Re_D.

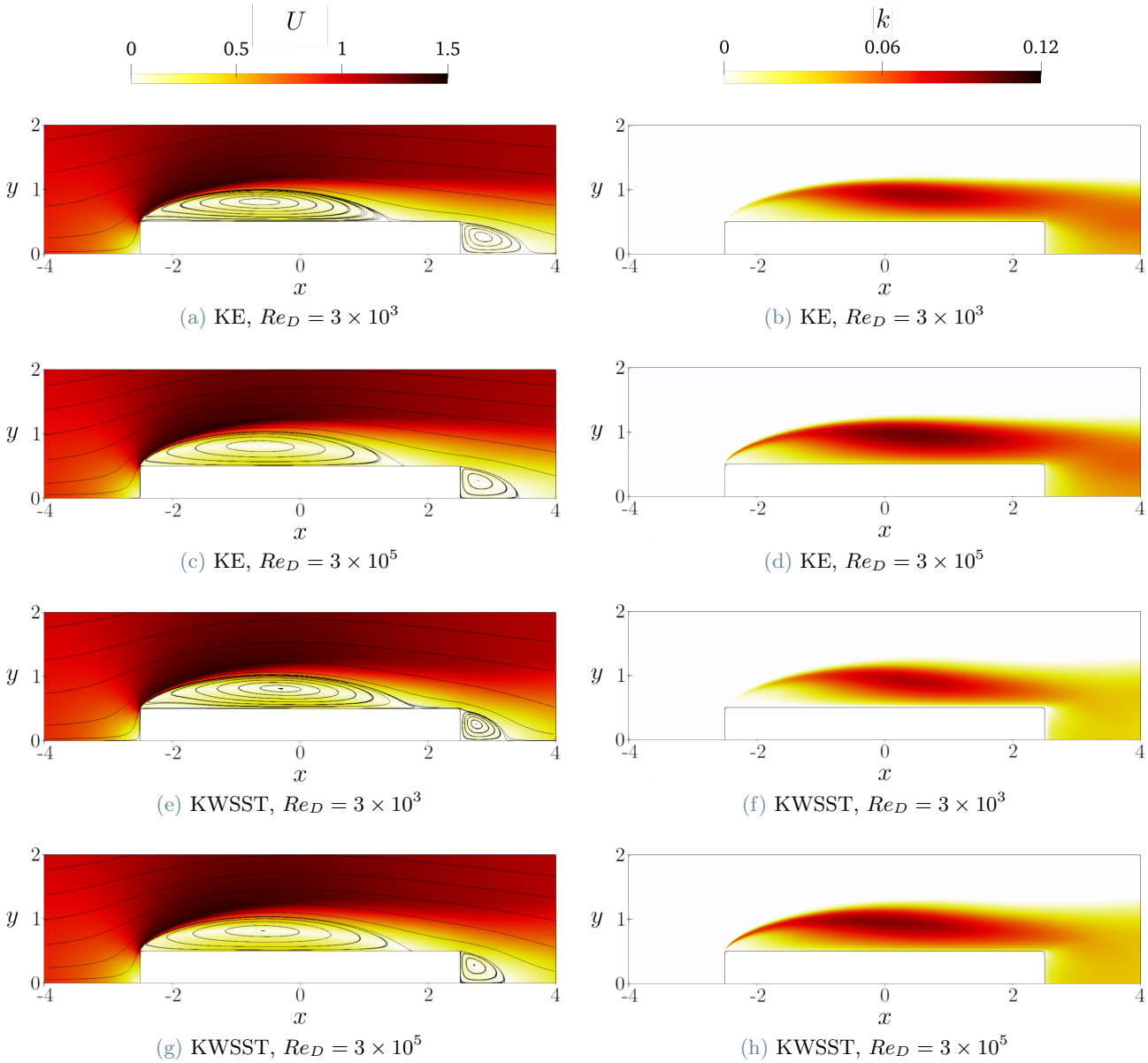

(a) KE, $Re_D = 3 \times 10^3$ (b) KE, $Re_D = 3 \times 10^3$

(c) KE, $Re_D = 3 \times 10^5$ (d) KE, $Re_D = 3 \times 10^5$

(e) KWSST, $Re_D = 3 \times 10^3$ (f) KWSST, $Re_D = 3 \times 10^3$

(g) KWSST, $Re_D = 3 \times 10^5$ (h) KWSST, $Re_D = 3 \times 10^5$

Figure 24: Comparison of the velocity and k colour map for the KE and KWSST model at two Re_D conditions.

The average drag coefficient over one period for the KE model is equal to $\langle C_d \rangle = 0.993$ showing an increase of 6.6% compared to the low Re case, this result approximates quite well the LES results at $Re_D = 4 \times 10^4$ for which $0.95 < \langle C_d \rangle < 1.00$ while it underestimates the result by Wei & Kareem (2011) for which $1.165 < \langle C_d \rangle < 1.305$ at $Re_D = 10^5$, a closer result to this last study is given by the KWSST model with $\langle C_d \rangle = 1.122$.
In conclusion the increase of Re number reduces the dimension and role of the laminar shear layer region that is one of the critical features that URANS simulations are unable to describe, for this reason the use of URANS simulations for the analysis of the BARC flow is more indicated for high Re flows. It should be noted that despite the increase in accuracy this type of simulations are still unable to correctly describe the composition

	DNS	KWSST	KE
P. vortex	$x_{s,1}$	-2.5	-2.5
	$x_{e,1}$	1.76	1.60
	L_1	4.26	4.10
	(x_c, y_c)	$(-0.58, 0.815)$	$(-0.627, 0.815)$
Wake vortex	$x_{s,3}$	2.5	2.5
	$x_{e,3}$	3.204	3.411
	L_3	0.704	0.911
	(x_c, y_c)	$(2.720, 0.281)$	$(2.782, 0.273)$

Table 13: Vortices positions for $Re = 3^5$

of the main recirculating region and identify the presence of two vortices. Given the Re difference between the URANS simulation and the four reference studies utilized, a set of high Re simulations ($Re > 10^5$), computed with more accurate methods such as LES, would be useful to better evaluate the accuracy of the turbulence models.

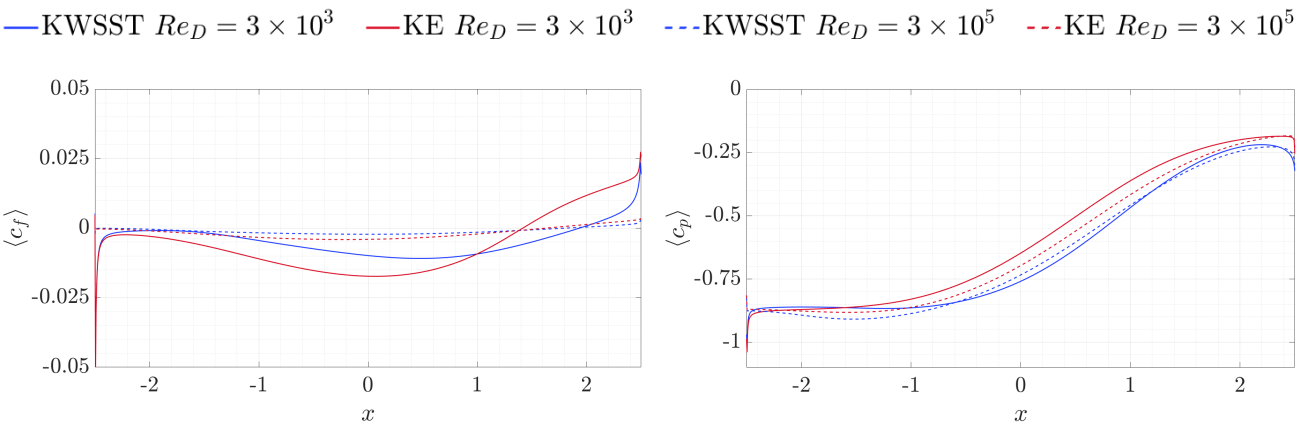

Figure 25: Friction and pressure coefficients along the cylinder's longitudinal side.

.

4. Conclusions

This study focused on the simulation of a the BARC geometry as a mean of evaluation of different turbulence models. The comparisons proposed for the various TKE budget terms offer useful information regarding the different abilities of these models in predicting specific flow features and highlights which regions of the flow or turbulent mechanisms are less accurately described by them, such as the laminar shear layer and the dissipation near the wall. This approach, that depends on availability of accurate simulations of complex flows as DNS simulations, can be an helpful tool in the development of new turbulence models and improvement of existing ones, highlighting the critical conditions that require more attention. Considering the specific case analyzed in this study, the performance in a low Re condition of the models implemented is mediocre, the main flow features as the primary separation and the vortex shedding frequency are inaccurately predicted with only the specific low Re Launder Sharma model capable of simulating important flow features as the laminar separation and the primary vortex shape in spite of the poor performance in the stagnation region and around the LE corners. Better accuracy is observed instead for the high Re case, the turbulence models obtain valid results compared to LES simulations and are capable of describing the most important flow structures.
In order to further develop the analysis of turbulence models applied to the BARC flow 3D simulations could be implemented. As presented in Section 3.3, the dissipation of turbulent kinetic energy requires the contribution of spanwise motions that cannot be captured by 2D simulations, the addition of the third dimension would allow the user to evaluate the turbulence models ability to predict these components.
We would like to thank T. Bellosta and E. Gallorini for their contribution to the development of the URANS simulations and of the budget terms analysis.

References

Aupoix, B., Arnal, D., Bézard, H., Chaouat, B., Chedevergne, F., Deck, S., Gleize, V., Grenard, P. & Laroche, E. 2011 Transition and Turbulence Modeling. *Aerospace Lab* **2**, 1–13.

Bardina, J., Huang, P. & Coakley, T. 1997 Turbulence Modeling Validation, Testing, and Development. *NASA Technical Memorandum* .

Bartoli, G., Borsani, A., Mannini, C., Marra, A. M., Procino, L. & Ricciardelli, F. 2011 Wind tunnel study on the aerodynamics of a 5: 1 rectangular cylinder in smooth flow. In *Proceedings of the Thirteenth International Conference on Wind Engineering, Amsterdam, The Netherlands*.

Bauer, J. & Tyacke, J. 2022 Comparison of low Reynolds number turbulence and conjugate heat transfer modelling for pin-fin roughness elements. *Applied Mathematical Modelling* **103**, 696–713.

Boussinesq, J. V. 1877 *Essai sur la théorie des eaux courantes*. Imprimeria nationale.

Bronkhorst, A.J., Geurts, C.P.W. & Bentum, C.A., van 2011 Unsteady pressure measurements on a 5:1 rectangular cylinder. In *13th International Conference on Wind Engineering*. Amsterdam.

Bruno, L., Fransos, D., Coste, N. & Bosco, A. 2008 3D flow around a rectangular cylinder: A computational study. *Journal of Wind Engineering and Industrial Aerodynamics* **98** (6), 263–276.

Bruno, L., Salvetti, M. V. & Ricciardelli, F. 2014 Benchmark on the Aerodynamics of a Rectangular 5:1 Cylinder: An overview after the first four years of activity. *Journal of Wind Engineering and Industrial Aerodynamics* **126**, 87–106.

Bush, R. H., Chyczewski, T., Duraisamy, K., Eisfeld, B., Rumsey, C. L. & Smith, B. R. 2019 Recommendations for Future Efforts in RANS Modeling and Simulation. In *AIAA SciTech 2019 Forum*. San Diego,CA.

Catalano, P. & Tognaccini, R. 2011 RANS analysis of the low-Reynolds number flow around the SD7003 airfoil. *Aerospace Science and Technology* **15** (8), 615–626.

Chiarini, A., Gatti, D., Cimarelli, A. & Quadrio, M. 2022 Structure of turbulence in the flow around a rectangular cylinder. *Journal of Fluid Mechanics* **946**.

Chiarini, A. & Quadrio, M. 2021 The Turbulent Flow over the BARC Rectangular Cylinder: A DNS Study. *Flow, Turbulence and Combustion* **107** (4), 875–899.

Chiarini, A. & Quadrio, M. 2022 The importance of corner sharpness in the BARC test case: A numerical study. *Wind and Structures* **34** (1), 43–58, arXiv: 2109.03522.

Cimarelli, A., Leonforte, A. & Angeli, D. 2018*a* Direct numerical simulation of the flow around a rectangular cylinder at a moderately high Reynolds number. *Journal of Wind Engineering and Industrial Aerodynamics* **174**, 39–49.

Cimarelli, A., Leonforte, A. & Angeli, D. 2018*b* On the structure of the self-sustaining cycle in separating and reattaching flows. *Journal of Fluid Mechanics* **857**, 907–936.

Cimarelli, A., Leonforte, A., De Angelis, E., Crivellini, A. & Angeli, D. 2019 On negative turbulence production phenomena in the shear layer of separating and reattaching flows. *Physics Letters A* **383** (10), 1019–1026.

Corsini, R., Angeli, D., Stalio, E., Chibbaro, S. & Cimarelli, A. 2022 Flow solutions around rectangular cylinders: The question of spatial discretization. *Wind and Structures* **34** (1), 151–159.

Crivellini, A., Nigro, A., Colombo, A., Ghidoni, A., Noventa, G., Cimarelli, A. & Corsini, R. 2022 Implicit Large Eddy Simulations of a rectangular 5:1 cylinder with a high-order discontinuous Galerkin method. *Wind and Structures* **34** (1), 59–72.

Delibra, G., Borello, D., Hanjalić, K. & Rispoli, F. 2009 URANS of flow and endwall heat transfer in a pinned passage relevant to gas-turbine blade cooling. *International Journal of Heat and Fluid Flow* **30** (3), 549–560.

Durbin, P.A. 1996 On the k-3 stagnation point anomaly. *International Journal of Heat and Fluid Flow* **17** (1), 89–90.

Edwards, J. R. & Chandra, S. 1996 Comparison of eddy viscosity-transport turbulence models for three-dimensional, shock-separated flowfields. *AIAA Journal* **34** (4), 756–763.

Franke, R. & Rodi, W. 1993 Calculation of Vortex Shedding Past a Square Cylinder with Various Turbulence Models. In *Turbulent Shear Flows 8*, pp. 189–204. Berlin, Heidelberg: Springer.

Grozescu, A. N., Bruno, L., Fransos, D. & Salvetti, M. V. 2011 Large-eddy simulations of a Benchmark on the Aerodynamics of a Rectangular 5: 1 Cylinder. In *Proceedings of the 20th Italian Conference on Theoretical and Applied Mechanics, Bologna, Italy*.

Jeong, J. & Hussain, F. 1995 On the identification of a vortex. *Journal of Fluid Mechanics* **285**, 69–94.

Launder, B. E., Reece, G. J. & Rodi, W. 1975 Progress in the development of a Reynolds-stress turbulence closure. *Journal of Fluid Mechanics* **68** (3), 537–566.

Launder, B. E. & Sharma, B. I. 1974 Application of the energy-dissipation model of turbulence to the calculation of flow near a spinning disc. *Letters in Heat and Mass Transfer* **1** (2), 131–137.

Launder, B. E. & Spalding, D. B. 1974 The numerical computation of turbulent flows. *Computer Methods in Applied Mechanics and Engineering* **3** (2), 269–289.

Li, W., Ren, J., Hongde, J., Luan, Y. & Ligrani, P. 2016 Assessment of six turbulence models for modeling and predicting narrow passage flows, part 2: Pin fin arrays. *Numerical Heat Transfer, Part A: Applications* **69** (5), 445–463.

Mannini, C., Mariotti, A., Siconolfi, L. & Salvetti, M. V. 2019 Benchmark on the Aerodynamics of a 5:1 Rectangular Cylinder: Further Experimental and LES Results. In *Direct and Large-Eddy Simulation XI*, pp. 427–432. Cham: Springer International Publishing.

Mannini, C., Marra, A., Pigolotti, L. & Bartoli, G. 2017 The effects of free-stream turbulence and angle of attack on the aerodynamics of a cylinder with rectangular 5:1 cross section. *Journal of Wind Engineering and Industrial Aerodynamics* **161**, 42–58.

Mannini, C., Soda, A. & Schewe, G. 2010 Unsteady RANS modelling of flow past a rectangular cylinder: Investigation of Reynolds number effects. *Computers & Fluids* **39**, 1609–1624.

Menter, F. R. 1994 Two-equation eddy-viscosity turbulence models for engineering applications. *AIAA Journal* **32** (8), 1598–1605.

Nguyen, D. T., Hargreaves, D. M. & Owen, J. S. 2018 Vortex-induced vibration of a 5:1 rectangular cylinder: A comparison of wind tunnel sectional model tests and computational simulations. *Journal of Wind Engineering and Industrial Aerodynamics* **175**, 1–16.

Ohya, Y. 2014 Bluff body flow and vortex—its application to wind turbines. *Fluid Dynamics Research* **46** (6), 061423.

Patruno, L., Ricci, M., de Miranda, S. & Ubertini, F. 2016 Numerical simulation of a 5:1 rectangular cylinder at non-null angles of attack. *Journal of Wind Engineering and Industrial Aerodynamics* **151**, 146–157.

Pope, S. B. 2000 *Turbulent Flows*. Cambridge University Press.

Ribeiro, A. FP 2011 Unsteady RANS modelling of flow past a rectangular 5: 1 cylinder: Investigation of edge sharpness effects. In *Proceedings of the 13th International Conference on Wind Engineering, Amsterdam, The Netherlands*.

Ricci, M., Patruno, L., de Miranda, S. & Ubertini, F. 2017 Flow field around a 5:1 rectangular cylinder using LES: Influence of inflow turbulence conditions, spanwise domain size and their interaction. *Computers & Fluids* **149**, 181–193.

Rocchio, B., Mariotti, A. & Salvetti, M. V. 2020 Flow around a 5: 1 rectangular cylinder: Effects of upstream-edge rounding. *Journal of Wind Engineering and Industrial Aerodynamics* **204**, 104237.

Rodi, W. 1997 Comparison of LES and RANS calculations of the flow around bluff bodies. *Journal of Wind Engineering and Industrial Aerodynamics* **69–71**, 55–75.

Sasaki, K. & Kiya, M. 1991 Three-Dimensional Vortex Structure in a Leading-Edge Separation Bubble at Moderate Reynolds Numbers. *Journal of Fluids Engineering* **113** (3), 405–410.

Schafer, M. 2006 *Computational Engineering — Introduction to Numerical Methods*. Berlin/Heidelberg: Springer-Verlag.

Schewe, G. 2013 Reynolds-number-effects in flow around a rectangular cylinder with aspect ratio 1:5. *Journal of Fluids and Structures* **39**.

Shimada, K. & Ishihara, T. 2002 Application of a modified k-ϵ model to the prediction of aerodynamic characteristics of rectangular cross-section cylinders. *Journal of Fluids and Structures* **16**, 465–485.

Shirato, H., Sato, Y., Sasaki, O. & Bao, D. 2010 Coherent structure of surface pressures on 2-D rectangular cylinders. *Earth and Space 2010: Engineering, Science, Construction, and Operations in Challenging Environments* .

Singh, A., Satheesh Kumar, A., Kubendiran, S. & B T, K. 2020 Assessment of Turbulence Models on a Backward Facing Step Flow Using OpenFOAM®. *IOP Conference Series: Materials Science and Engineering* **912**.

Spalart, P. & Allmaras, S. 1992 A One-Equation Turbulence Model for Aerodynamic Flows. *AIAA Journal* **439**.

Spalart, P. R 2000 Strategies for turbulence modelling and simulations. *International Journal of Heat and Fluid Flow* **21** (3), 252–263.

Spalart, P. R. & Shur, M. L. 2000 Turbulence Modeling in Rotating and Curved Channels: Assessing the Spalart-Shur Correction. *AIAA Journal* **38** (5).

Sun, W., Jo, S. & Seok, Jongwon 2019 Development of the optimal bluff body for wind energy harvesting using the synergetic effect of coupled vortex induced vibration and galloping phenomena. *International Journal of Mechanical Sciences* **156**, 435–445.

Wei, Z. & Kareem, A. 2011 A benchmark study of flow around a rectangular cylinder with aspect ratio 1:5 at Reynolds number 1.E5. In *Proceedings of the Thirteenth International Conference on Wind Engineering, Amsterdam, The Netherlands.*.

Wilcox, D. C. 2006 *Turbulence Modeling for CFD*, 3rd edn. La Cañada, Calif.: D C W Industries.

Williams, O., Samuell, M., Sarwas, E. S., Robbins, M. & Ferrante, A. 2020 Experimental Study of a CFD Validation Test Case for Turbulent Separated Flows. In *AIAA Scitech 2020 Forum*. American Institute of Aeronautics and Astronautics.

Xiao-bing, L. I. U., Hai-dong, Z. & Yan-biao, W. 2015 Study On Spanwise Correlation Of Aerodynamic Force of Rectangular Cylinder with Aspect Ratio 5. *Engineering Mechanics* **32**, 50–54.

Yan, C., Li, H., Zhang, Yufei & Chen, Haixin 2022 Data-driven turbulence modeling in separated flows considering physical mechanism analysis. *International Journal of Heat and Fluid Flow* **96**, 109004.

Zhang, Q. & Yang, Y. 2013 A new simpler rotation/curvature correction method for Spalart–Allmaras turbulence model. *Chinese Journal of Aeronautics* **26** (2), 326–333.

Zhang, Z. & Xu, F. 2020 Spanwise length and mesh resolution effects on simulated flow around a 5:1 rectangular cylinder. *Journal of Wind Engineering and Industrial Aerodynamics* **202**, 104–186.

A. Turbulence Models

Four turbulence models have been implemented in the 2D URANS simulations presented in this study, they are: $k-\epsilon$ (Launder *et al.*, 1975) (hereafter indicated with KE), Launder Sharma $k-\epsilon$ (Launder & Sharma, 1974) (LSKE), $k-\omega$ SST (Menter, 1994) (KWSST) and the Spalart Allmaras with Rotational/Curvature corretction developed by Zhang & Yang (2013) (SARC). All the turbulence models are based on the turbulent viscosity hypothesis firstly introduced in Boussinesq (1877) in order to relate the Reynolds stresses contribution to the mean flow characteristics.
Considering the velocity field decomposed with the standard Reynolds decomposition, each velocity component $\boldsymbol{u_i}$ is given by the sum of its mean and fluctuating parts $\boldsymbol{u_i} = \overline{\boldsymbol{u_i}} + \boldsymbol{u_i'}$. The turbulent viscosity hypothesis can be seen as two assumptions: the first one is that the Reynolds-stress anisotropy $a_{ij} = \overline{u_i' u_j'} - \frac{2}{3}k\delta_{ij}$ with $k = \frac{1}{2}\overline{u_i' u_i'}$ is determined by the mean velocity gradient $\frac{\partial \overline{\boldsymbol{u_i}}}{\partial x_j}$; the second consists in relating the two elements through the use of the turbulent viscosity ν_t.

$$a_{ij} = -\nu_t \left(\frac{\partial \overline{\boldsymbol{u_i}}}{\partial x_j} + \frac{\partial \overline{\boldsymbol{u_j}}}{\partial x_i} \right) \tag{14}$$

A.1. KE

The KE turbulence model, introduced by Launder & Spalding (1974), is a two equation model in which the transport equations for the turbulent kinetic energy k and dissipation ϵ are solved. These two quantities can be utilized to define a lengthscale, a timescale and a quantity of dimension k^2/ϵ. For this reason it is a complete model that does not require the definition of a mixing length $l_m(x)$. In addition to the two model equations the turbulent viscosity is expressed as $\nu_t = C_\mu(k^2/\epsilon)$. The two equations, respectively for the turbulent kinetic dissipation and energy, are the following:

$$\begin{cases} \dfrac{D\epsilon}{Dt} = \dfrac{1}{\rho}\dfrac{\partial}{\partial x_k}\left[\dfrac{\nu_t}{\sigma_\epsilon}\dfrac{\partial \epsilon}{\partial x_k}\right] + \dfrac{C_1 \nu_t}{\rho}\dfrac{\epsilon}{k}\left(\dfrac{\partial u_i}{\partial x_k} + \dfrac{\partial u_k}{\partial x_i}\right)\dfrac{\partial u_i}{\partial x_k} - C_2\dfrac{\epsilon^2}{k} \\ \dfrac{Dk}{Dt} = \dfrac{1}{\rho}\dfrac{\partial}{\partial x_k}\left[\dfrac{\nu_t}{\sigma_k}\dfrac{\partial k}{\partial x_k}\right] + \dfrac{\nu_t}{\rho}\left(\dfrac{\partial u_i}{\partial x_k} + \dfrac{\partial u_k}{\partial x_i}\right)\dfrac{\partial u_i}{\partial x_k} - \epsilon \end{cases} \tag{15}$$

where
$C_1 = 1.44$
$C_2 = 1.92$
$C_\mu = 0.09$
$\sigma_\epsilon = 1.3$
$\sigma_k = 1.0$

A.2. LSKE

The LSKE model is a modification of the standard KE model, introduced to overcome the limitations in the simulation of wall bounded flows and the effect of viscosity in the near wall region. To do so a new set of coefficients and damping functions have been introduced: f_μ, f_1, f_2, D and E. The turbulent viscosity is calculated as $\nu_t = C_\mu f_\mu(k^2/\epsilon)$. The following are the turbulent kinetic dissipation and energy transport equations:

$$\begin{cases} \dfrac{D\epsilon}{Dt} = \dfrac{1}{\rho}\dfrac{\partial}{\partial x_k}\left[\dfrac{\nu_t}{\sigma_\epsilon}\dfrac{\partial \epsilon}{\partial x_k}\right] + \dfrac{C_1 f_1 \nu_t}{\rho}\dfrac{\epsilon}{k}\left(\dfrac{\partial u_i}{\partial x_k} + \dfrac{\partial u_k}{\partial x_i}\right)\dfrac{\partial u_i}{\partial x_k} - C_2 f_2\dfrac{\epsilon^2}{k} + E \\ \dfrac{Dk}{Dt} = \dfrac{1}{\rho}\dfrac{\partial}{\partial x_k}\left[\dfrac{\nu_t}{\sigma_k}\dfrac{\partial k}{\partial x_k}\right] + \dfrac{\nu_t}{\rho}\left(\dfrac{\partial u_i}{\partial x_k} + \dfrac{\partial u_k}{\partial x_i}\right)\dfrac{\partial u_i}{\partial x_k} - \epsilon - D \end{cases} \tag{16}$$

where
$C_1 = 1.44$
$C_2 = 1.92$
$C_\mu = 0.09$
$\sigma_\epsilon = 1.3$
$\sigma_k = 1.0$
$Re_T = \frac{k^2}{\nu\epsilon}$
$f_\mu = exp[-3.4/(1 + Re_T/50)^2]$
$f_1 = 1$

$f_2 = 1 - 0.3exp(-Re_T^2)$
$D = 2\nu \left(\frac{\partial\sqrt{k}}{\partial y}\right)^2$
$E = 2\nu\nu_t \left(\frac{\partial^2 u}{\partial y^2}\right)^2$

A.3. KWSST

The $k-\omega$ SST model implemented in this study is derived by the standard $k-\omega$ turbulence model introduced in Wilcox (2006). This model, superior to the standard $k-\epsilon$ in the near wall regions and in accounting for the effect of streamwise pressure gradients, is however limited in the treatment of free-stream non-turbulent boundaries. Menter (1994) proposed a modification to the Wilcox model taking advantage of the strengths of both the $k-\epsilon$ and $k-\omega$ with the use of a blending function. This model, called $k-\omega$ SST, enforces the $k-\omega$ formulation near the walls and transitions to the $k-\epsilon$ model away from them. The following equations, for the turbulent dissipation rate and energy, are the 2003 version of the model, which has few small modifications from the original one.

$$\begin{cases} \dfrac{\partial(\rho\omega)}{\partial t} + \dfrac{\partial(\rho u_i\omega)}{x_j} = \dfrac{\gamma}{\nu_t}P - \beta\rho\omega^2 + \dfrac{\partial}{\partial x_j}\left[(\mu+\sigma_\omega\mu_t)\dfrac{\partial\omega}{\partial x_j}\right] + 2(1-F_1)\dfrac{\rho\sigma_{\omega 2}}{\omega}\dfrac{\partial k}{\partial x_j}\dfrac{\partial\omega}{\partial x_j} \\ \dfrac{\partial(\rho k)}{\partial t} + \dfrac{\partial(\rho u_j k)}{\partial x_j} = P - \beta^*\rho\omega k + \dfrac{\partial}{\partial x_j}\left[(\mu+\sigma_k\mu_t)\dfrac{\partial k}{x_j}\right] \end{cases} \tag{17}$$

With the turbulent viscosity computed as:

$$\mu_t = \frac{\rho a_1 k}{max(a_1\omega, SF_2)} \quad with \quad S \quad = \sqrt{2S_{ij}S_{ij}} \tag{18}$$

where

$P = \tau_{ij}\frac{\partial u_i}{\partial x_j}$ limited in both equation by $min(P, 10\beta^*\rho\omega k)$
$\tau_{ij} = \mu_t(2S_{ij} - \frac{2}{3}\frac{\partial u_k}{\partial x_k}\delta_{ij}) - \frac{2}{3}\rho k\delta_{ij}$
$S_{ij} = \frac{1}{2}\left(\frac{\partial u_i}{\partial x_j} + \frac{\partial u_i}{\partial x_i}\right)$
$F_1 = tanh(arg_1^4)$
$arg_1 = min\left[max\left(\frac{\sqrt{k}}{\beta^*\omega d}, \frac{500\nu}{d^2\omega}\right), \frac{4\rho\sigma_{\omega 2}k}{CD_{k\omega}d^2}\right]$
$CD_{k\omega} = max\left(2\rho\sigma_{\omega 2}\frac{1}{\omega}\frac{\partial k}{\partial x_j}\frac{\partial\omega}{\partial x_j}, 10^{-10}\right)$
$F_2 = tanh(arg_2^2)$
$arg_2 = max\left(2\frac{\sqrt{k}}{\beta^*\omega d}, \frac{500\nu}{d^2\omega}\right)$
$\nu_t = \mu_t/\rho$

$\gamma_1 = 5/9$
$\gamma_2 = 0.44$
$\sigma_{k1} = 0.85$
$\sigma_{k2} = 1.0$
$\sigma_{\omega 1} = 0.5$
$\sigma_{\omega 2} = 0.856$
$\beta_1 = 0.075$
$\beta_2 = 0.0828$
$\beta^* = 0.09$
$\kappa = 0.41$
$a_1 = 0.31$

The blending between the near wall constants and those indicated for the region of the flow away from the wall is obtained in the following way, in which ϕ represents the generic constant:

$$\phi = F_1\phi_1 + (1-F_1)\phi_2 \tag{19}$$

A.4. SARC

The modification of the standard one equation Spalart Allmaras model (Spalart & Allmaras, 1992) implemented in this study is the Simpler Rotational/Curvature Correction proposed by Zhang & Yang (2013). It delivers very similar accuracy to the standard Spalart-Shure rotational correction (Spalart & Shur, 2000) with a lower computational cost. The single equation implemented is utilized to model the evolution of the turbulent field unknown $\hat{\nu}$ is here presented:

$$\frac{\partial\hat{\nu}}{\partial t} + u_j\frac{\partial\hat{\nu}}{\partial x_j} = c_{b1}f_{r1}(1-f_{t2})\hat{S}\hat{\nu} - \left[c_{w1}f_w - \frac{c_{b1}}{\kappa^2}f_{t2}\right]\left(\frac{\hat{\nu}}{d}\right)^2 + \frac{1}{\sigma}\left[\frac{\partial}{\partial x_j}\left((\nu+\hat{\nu})\frac{\partial\hat{\nu}}{\partial x_j}\right) + c_{b2}\frac{\partial\hat{\nu}}{\partial x_i}\cdot\frac{\partial\hat{\nu}}{\partial x_i}\right] \tag{20}$$

where

d is the distance from the nearest wall
$f_w = g\left(\frac{1+c_{w3}^6}{g^6+c_{w3}^6}\right)$
$g = r + c_{w2}(r^6 - r)$
$r = min\left(\frac{\hat{\nu}}{\hat{S}\kappa^2 d^2}, 10\right)$
$f_{t2} = c_{t3} exp(-c_{t4}\xi^2)$
$c_{b1} = 0.1355$
$c_{b2} = 0.622$
$\sigma = 2/3$

$\kappa = 0.41$
$\gamma_2 = 0.44$
$c_{w1} = \frac{c_{b1}}{\kappa^2} + \frac{1+c_{b2}}{\sigma}$
$c_{w2} = 0.3$
$c_{w3} = 2$
$c_{t3} = 1.2$
$c_{t4} = 0.5$
$c_{v1} = 7.1$

The empirical rotation term introduced in this correction, f_{r1}, is defined as:

$$f_{r1}(r^*, \bar{r}) = (1 + c_{r1})\frac{2r^*}{r^* + 1}[1 - c_{r3} arctan(c_{r2}\tilde{r})] - c_{r1} \tag{21}$$

where

$\tilde{r} = \frac{\Omega}{S}\left(\frac{\Omega}{S} - 1\right)$
$r^* = S/\Omega$
$S = \sqrt{2S_{ij}S_{ij}}$
$S_{ij} = \frac{1}{2}\left(\frac{\partial u_i}{\partial x_j} + \frac{\partial u_j}{\partial x_i}\right)$
$\Omega = \sqrt{2W_{ij}W_{ij}}$
$W_{ij} = \frac{1}{2}\left[\left(\frac{\partial u_i}{\partial x_j} - \frac{\partial u_j}{\partial x_i}\right) + 2\epsilon_{mij}\Omega'_m\right]$

$c_{r1} = 1$
$c_{r2} = 12$
$c_{r3} = 0.6$

The turbulent viscosity is the calculated as:

$$\mu_t = \rho\hat{\nu} f_{v1} \tag{22}$$

where

$$\begin{cases} f_{v1} = \dfrac{\chi^3}{\chi^3 + c_{v1}^3} \\ \chi = \dfrac{\hat{\nu}}{nu} \end{cases} \tag{23}$$

and
$\hat{S} = \Omega + \frac{\hat{\nu}}{k^2 d^2} f_{v2}$
$f_{v2} = 1 - \frac{\chi}{1+\chi f_{v1}}$

B. Grid independence study

In order to establish the results' independence from the mesh characteristics, different simulations were completed for each turbulence model at different levels of mesh refinement. For the KE, KWSST and SARC models the meshes utilised, described in Section 2 consist of 60758, 121920 and 245952 elements while for the LSKE they consist of 739524, 106108 and 145276 elements, in both cases the y^+ maximum value is below 1. For the simulations at $Re = 3 \cdot 10^5$ the meshes consist of 133068, 212296 and 358322 elements with a maximum $y^+ \approx 2.5$. In Figures 26-27 values of the $\langle c_p \rangle$ coefficients along the cylinder body for all the selected mesh refinements are presented to demonstrate the convergence of the simulations results for each of turbulence models. In addition to the variation of pressure coefficient profile, the change of drag coefficient between the highest refinement and the previous refinement level has been considered in order to establish the similarity of the two solutions. These differences at $Re = 3000$ amount to 1.4% for the KE model, 1.6% for the LSKE model, 0.2% for the KWSST model and 0.1% for the SARC model that requires two different mesh refinements to exhibit grid independence. In the $Re = 3 \times 10^5$ this difference is of 1.3% for the KE model and 0.4% for the KWSST model.

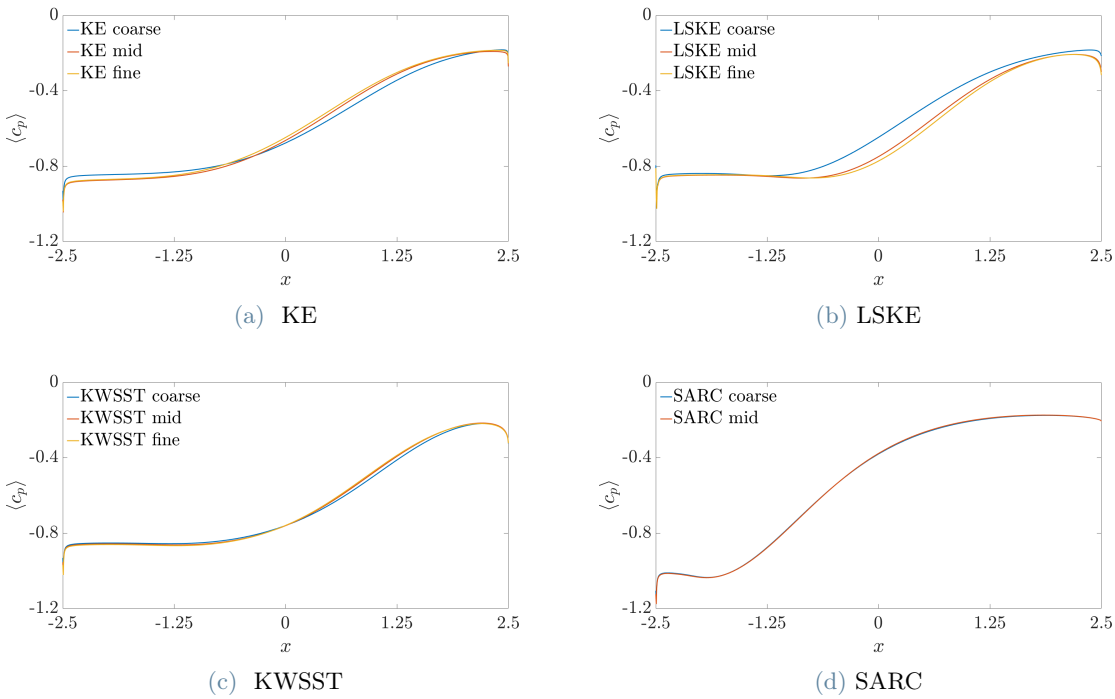

(a) KE (b) LSKE

(c) KWSST (d) SARC

Figure 26: $\langle c_p \rangle$ profiles on different meshes at $Re = 3 \times 10^3$

.

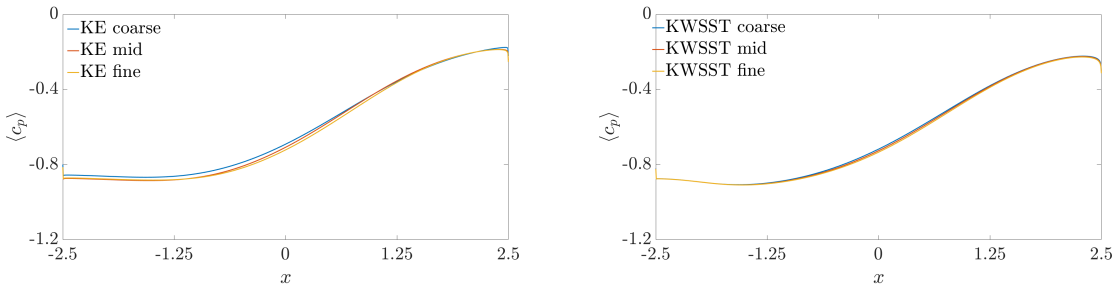

(a) $k - \epsilon$ (b) LS $k - \omega$

Figure 27: $\langle c_p \rangle$ profiles on different meshes at $Re = 3 \times 10^5$

Abstract in lingua italiana

In questo studio vengono analizzate le capacita di modelli RANS nel simulare il flusso turbolento intorno ad un prisma rettangolare con rapporto corda-spessore pari a 5:1, altresì noto come BARC benchmark, al numero di Reynolds relativamente basso di $Re = 3000$. Sono considerati quattro modelli di turbolenza e la loro performance è comparata con i risultati DNS disponibili. Nonostante la semplicità della geometria questo flusso è particolarmente impegnativo poiché presenta una separazione laminare, uno shear layer instabile, strati limite allineati al flusso e inversi e alcune zone di ricircolo. I modelli RANS considerati predicono sufficientemente bene il coefficiene di drag ma falliscono nel determinare le principali caratteristiche del flusso. Alcuni modelli falliscono anche nella predizione del rilascio di vortici nella scia. I termini della equazione del budget dell'energia cinetica turbolenta sono utilizzati per valutare criticamente la performance dei modelli e evidenziare i loro limit. Tali informazioni sono utili per la regolazione e lo sviluppo di modelli di turbolenza per flussi complessi con separazione e riattacco.

Parole chiave: Modelli di turbolenza, corpi tozzi, URANS